Drag force in granular shear flows: Regimes, scaling laws, and implications for segregation

Lu Jing[1,4], Julio M. Ottino[1,2,3], Paul B. Umbanhowar[2], and Richard M. Lueptow[1,2,3]†

[1]Department of Chemical and Biological Engineering, Northwestern University, Evanston, IL 60208, USA

[2]Department of Mechanical Engineering, Northwestern University, Evanston, IL 60208, USA

[3]Northwestern Institute on Complex Systems (NICO), Northwestern University, Evanston, IL 60208, USA

[4]Institute for Ocean Engineering, Shenzhen International Graduate School, Tsinghua University, Shenzhen 518055, China

(Received xx; revised xx; accepted xx)

The drag force on a spherical intruder in dense granular shear flows is studied using discrete element method simulations. Three regimes of the intruder dynamics are observed depending on the magnitude of the drag force (or the corresponding intruder velocity) and the flow inertial number: a fluctuation-dominated regime for small drag forces, a viscous regime for intermediate drag forces, and an inertial (cavity formation) regime for large drag forces. The transition from the viscous regime (linear force-velocity relation) to the inertial regime (quadratic force-velocity relation) depends further on the inertial number. Despite these distinct intruder dynamics, we find a quantitative similarity between the intruder drag in granular shear flows and the Stokesian drag on a sphere in a viscous fluid for intruder Reynolds numbers spanning five orders of magnitude. Beyond this first-order description, a modified Stokes drag model is developed that accounts for the secondary dependence of the drag coefficient on the inertial number and the intruder size and density ratios. When the drag model is coupled with a segregation force model for intruders in dense granular flows, it is possible to predict the velocity of gravity-driven segregation of an intruder particle in shear flow simulations.

1. Introduction

Drag in granular media has significant implications for granular rheology (Nichol *et al.* 2010; Reddy *et al.* 2011), particle segregation (Tripathi & Khakhar 2011), impact and penetration mechanics in granular beds (Clark *et al.* 2014; Seguin *et al.* 2013), and even animal and robotic locomotion (Gravish *et al.* 2010; Li *et al.* 2013). Despite extensive research on the drag on intruder objects in static or vibrofluidized granular beds (e.g., Albert *et al.* 1999; Geng & Behringer 2005; Candelier & Dauchot 2009; Seguin & Gondret 2017), much less effort has focused on intruder drag in flowing granular materials. Yet, accurate drag models are essential to represent interspecies resistive forces and momentum exchange for multi-species granular flows, where the particle species differ in size, density, or other physical properties. In particular, drag is a key ingredient in various continuum models of segregation phenomena in multi-species granular flows (Jenkins & Yoon 2002; Gray 2018; Umbanhowar *et al.* 2019; Thornton 2021), where distinct particle

† Email address for correspondence: r-lueptow@northwestern.edu

species tend to segregate spontaneously and exert an effective drag force on each other. Current segregation models usually consider drag indirectly, e.g., via advection-diffusion equations incorporating a phenomenological segregation flux term, but the fundamental aspects of the drag in segregation flux behaviours remain unclear.

Recent studies of single intruder particles in otherwise species-monodisperse granular flows have provided significant particle-level insights into the mechanics of granular segregation (Tripathi & Khakhar 2011; Guillard *et al.* 2016; van der Vaart *et al.* 2018; Jing *et al.* 2020, 2021; Duan *et al.* 2022). An intruder particle differing in size or density in a granular flow tends to migrate across streamlines (rising or sinking), perhaps the simplest scenario for studying the forces relevant to granular segregation. However, even in this simple scenario, characterizing the forces on migrating intruders is non-trivial because granular flow-driven intruder migration is almost always in near-equilibrium conditions and, as a result, any measurable net contact force on the intruder is difficult to differentiate from the intruder weight (Staron 2018). Therefore, it is useful to partition the net contact force into components, such as buoyancy, lift, and drag forces, in analogy to the forces experienced by a particle migrating in ordinary fluids. In a recently developed approach, an intruder particle is tethered to a virtual spring in discrete element method (DEM) simulations (Guillard *et al.* 2016; van der Vaart *et al.* 2018; Jing *et al.* 2021; Liu & Müller 2021) to prevent segregation and eliminate the mean relative velocity between the intruder and the flow (so as to eliminate the effective drag force). In this way, it is possible to evaluate the net driving force of segregation for various flow conditions and particle properties. Although several different models have been proposed (Guillard *et al.* 2016; van der Vaart *et al.* 2018; Jing *et al.* 2021; Liu & Müller 2021), it is common that the net segregation force consists of a buoyancy-like term proportional to the pressure gradient and a kinematics-related term accounting for shear-induced effects due to the granular flow. Our recent model (Jing *et al.* 2020, 2021), which partitions the segregation force into a pressure-gradient term and a shear-rate-gradient term, accurately predicts when intruder particles will rise or sink in various confined and free-surface flow simulations and experiments over a wide range of particle size and density ratios.

In contrast to these advances in understanding the driving forces of segregation in the intruder regime, the resistive drag force during segregation remains largely unexplored. Previous studies (Tripathi & Khakhar 2011; Liu & McCarthy 2017; Duan *et al.* 2020; Bancroft & Johnson 2021) focus mainly on the drag force in density-bidisperse but size-monodisperse granular flows, or with a narrow range of size-bidispersity (Bancroft & Johnson 2021), but a general picture of how the intruder particle size, particle density, and flow conditions affect the drag force has not yet been developed. Tripathi & Khakhar (2011) found that the drag force on a few heavy intruders settling under gravity in inclined chute flow simulations follows Stokes' drag law, provided that the granular rheology is expressed in terms of an effective viscosity of the granular flow. The dimensionless drag coefficient further depends on the local inertial number (Tripathi & Khakhar 2013). Liu & McCarthy (2017) studied the settling of a few heavy intruders in simple shear simulations (where gravity acts only on the intruder particles to induce sedimentation) and found non-Stokesian behaviours in that the segregation velocity is not linearly correlated with the particle density ratio. They proposed an alternative viscosity model based on kinetic theory to collapse their data for various density ratios and flow conditions. More recently, Duan *et al.* (2020) and Bancroft & Johnson (2021) found similar power-law dependence of the interspecies drag on the inertial number (with exponents of -2 and $-7/4$, respectively) based on simulations of sheared density-bidisperse mixtures. Duan *et al.* (2020) also demonstrated that a kinetic theory-based drag model and the Stokesian drag model are approximately equivalent, as the role of velocity fluctuations can be captured by either the inertial number or the effective viscosity of the mixture flow. However, the relevance of these drag models for density-bidisperse mixtures with a finite particle species concentration is unclear in the single intruder regime. More importantly, the influence of particle size on the drag force has not been systematically studied.

Here, the approach we adopt to shed light on the fundamental characteristics of drag in flowing granular materials is the following. Using DEM simulations, we characterize the effective net resistive (drag) force on single intruder particles of different sizes and densities as they are displaced across streamlines in simple-shear granular flows. The use of simple shear (where stress and shear rate fields are homogeneous) avoids segregation forces induced by pressure- and shear-gradients (Guillard *et al.* 2016; Jing *et al.* 2021). Instead of increasing the intruder weight to induce sedimentation (Tripathi & Khakhar 2011; Liu & McCarthy 2017), we apply an external force on the intruder, independent of the mass, to displace it perpendicular to the shear. By systematically varying the flow conditions (shear rate and overburden pressure) and particle properties (size and density), we find a wide range of conditions where the mean steady-state intruder velocity is effectively constant (i.e., the applied force on the intruder is balanced by the net resistive drag force exerted by its neighbouring bed particles) and the scaling relation between the intruder velocity and the effective drag force is explored. This leads to a modified Stokesian drag model, which, when combined with our recent segregation force model (Jing *et al.* 2021), accurately predicts the dependence of the intruder segregation velocity on various parameters in gravity-driven segregation simulations.

2. Methods

2.1. *Shear flow setup*

The flow consists of a three-dimensional streamwise (x) and spanwise (y) periodic domain confined by two rough walls in the depthwise (z) direction (figure 1a), where the walls are roughened by randomly distributed stationary particles (Jing *et al.* 2016). The lower wall is stationary, while the upper wall translates in x with a velocity $U_0 = \dot{\gamma}_0 h$, where $\dot{\gamma}_0$ is the shear rate and $h = h(t)$ is the instantaneous flow depth which varies slightly in time t, and is reactive in z to maintain a constant overburden pressure P_0. Gravity is not present ($g = 0$) in simple shear simulations, but we show below that our findings remain valid when gravity is included. The domain is typically $20d$ long, $20d$ wide, and $35d$ deep (approximately 15000 spherical particles per simulation), where d is the mean bed particle diameter (with $\pm 10\%$ uniform polydispersity). We have increased the domain size to confirm that it is sufficiently large to avoid boundary effects.

To ensure homogeneous shear in each simulation, which does not otherwise occur under all simulation conditions due to possible shear localization near the moving wall, we apply a small streamwise stabilizing force $F_s = K_s[u(z_p) - u_p]$ to each particle (except the intruder particle) at each DEM simulation time step to maintain the desired linear flow velocity profile, $u(z) = \dot{\gamma}_0 z$, where u_p and z_p are instantaneous particle velocity and position, respectively, and K_s is a constant (Lerner *et al.* 2012; Clark *et al.* 2018; Fry *et al.* 2018; Jing *et al.* 2020, 2021). The appropriate value of K_s to avoid altering the granular flow rheology and yet ensure a linear velocity profile depends on P_0 and $\dot{\gamma}_0$ (Fry *et al.* 2018). We provide a detailed scaling analysis of K_s in Appendix A. Based on that analysis, we set the dimensionless version of this parameter to be $\tilde{K}_s = K_s \dot{\gamma}_0 I^{-0.25}/(P_0 d) = 0.1$ for all simulations, where $I = \dot{\gamma}_0 d/\sqrt{P_0/\rho}$ is the inertial number and ρ is the particle density. This choice produces satisfactorily homogeneous flows while not altering the flow

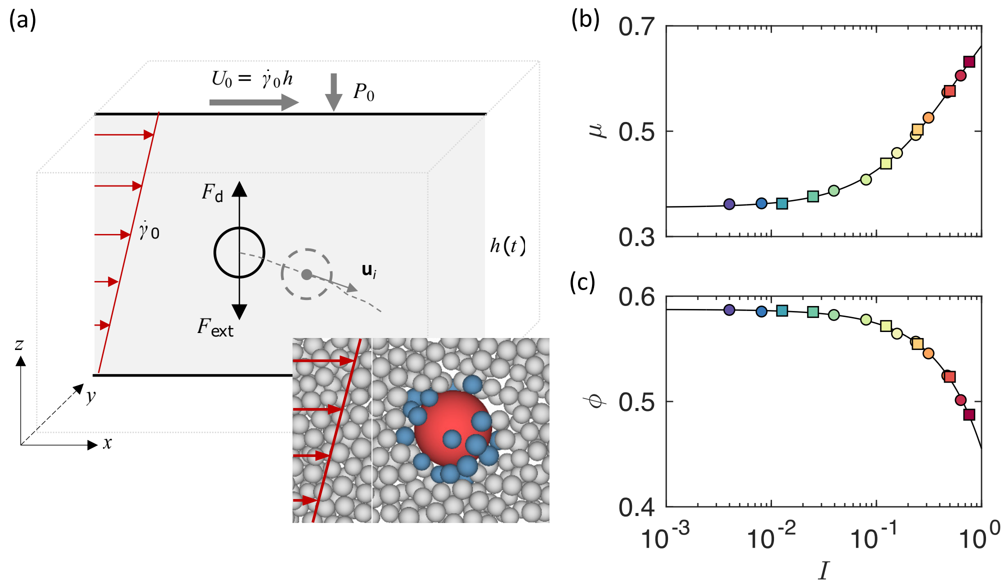

FIGURE 1. (a) Simulation setup and schematic trajectory of an intruder particle (not to scale). The inset shows a sinking intruder (red) and its contacting (blue) and non-contacting (grey) neighbouring particles in a small section of the flow. (b,c) Rheological data measured in the flow for $10 \leqslant z/d \leqslant 20$ for various simulations. Square and circle symbols represent $P_0 = 100$ Pa and 1000 Pa, respectively, and the colour from blue to red indicates increasing I (see text for range of $\dot{\gamma}_0$). Solid curves in (b) and (c) are described by $\mu(I) = 0.36 + 0.55/(0.73/I + 1)$ and $\phi(I) = 0.59 - 0.14I$, respectively.

rheology and drag behaviours; increasing or decreasing $\tilde{K}_s$ by a factor of ten does not affect the results (see Appendix A).

We focus on the dense granular flow regime, characterized by the inertial number I ranging approximately from 10^{-3} to 1, to avoid possible nonlocal effects for $I \lesssim 10^{-3}$ (Kim & Kamrin 2020) and the dilute, collisional flow regime for $I \gtrsim 1$ (Rognon & Macaulay 2021). To achieve this range of I, we use $\dot{\gamma}_0 = \{0.5, 1, 5, 10, 20, 30, 40, 60, 80\}$ s^{-1} for $P_0 = 1000$ Pa and $\dot{\gamma}_0 = \{0.5, 1, 5, 10, 20, 30\}$ s^{-1} for $P_0 = 100$ Pa. Bed particle properties are $d = 5$ mm and $\rho = 2500$ kg/m^3, but we vary d and ρ to confirm the scaling associated with I. Figures 1(b,c) show the rheological data, including the effective friction μ and average solid packing density ϕ, measured in a $10d$-thick layer in the middle of the flow, which follow the $\mu(I)$ and $\phi(I)$ relations typical of dense granular flows (Forterre & Pouliquen 2008). For the DEM simulations, we use the Hertz contact model with Young's modulus 5×10^7 Pa, Poisson's ratio 0.4, coefficient of restitution 0.8, and coefficient of friction 0.5. Note that using a linear contact model should produce similar results based on previous studies using the model for segregation in dense granular flows (Jing *et al.* 2020; Duan *et al.* 2022). The simulation time step is 10^{-5}s to assure numerical stability, and the results are insensitive to the contact parameters except for particle friction coefficients $\lesssim 0.3$, in agreement with previous studies (Tripathi & Khakhar 2011; Jing *et al.* 2020; Duan *et al.* 2020; Bancroft & Johnson 2021).

2.2. *Intruder particles and drag measurement*

We study drag on a small number of spherical intruder particles in the flow (see figure 1a), with a range of size ratios $R = d_i/d$ from 0.6 to 5 and density ratios $R_\rho =$

ρ_i/ρ from 1 to 20, where d_i and ρ_i are the intruder diameter and density, respectively. Typically, five intruders are included in each simulation to obtain statistically significant results, and we verify that the intruders are far enough apart that they do not interact with each other, a situation shown to occur at intruder particle concentrations below a finite critical concentration (Duan *et al.* 2022). However, for $R > 2$, the domain size needs to be at least doubled compared to that for $R = 1$ to accommodate multiple non-interacting intruders (Pacheco-Vázquez & Ruiz-Suárez 2010), which is computationally expensive, so we only use one intruder per simulation for $R > 2$. Nevertheless, we confirm that this is statistically sufficient because fluctuations associated with the random action of particle contacts decreases significantly for large R due to the rapid increase in the number of contacts with the intruder (which grows as R^2).

Each intruder is dragged by a constant external force F_{ext} imposed in the negative z-direction but is free to move with the flow in the x- and y-directions, as illustrated in figure 1(a). We have verified that dragging the intruder upward (in the absence of gravity) produces similar results. The net resistive drag force, F_d, i.e., the net force exerted on the intruder by bed particle contacts in the z-direction, is simply $F_d = F_{ext}$. The force balance is justified because the intruder migration is, on average, always in equilibrium; that is, we observe negligible net intruder acceleration in all simulations. For each applied F_{ext}, the corresponding mean (downward) intruder velocity, w_i, is determined based on the vertical trajectories of all intruders in a simulation as they pass through the flow depth from $z = 20d$ to $10d$ (typically encompassing about 50 snapshots over the time for the intruder to transit this distance; see plots of the intruder position vs. time in §3.1), thereby avoiding effects related to the lower or upper walls (Stone *et al.* 2004). Then, we analyse the relationship between F_d and w_i for a series of simulations with varying F_{ext}. Note that F_d acts in the opposite direction of w_i, but the signs of F_d and w_i are omitted here for simplicity. The situation is analogous to the relation between the drag force on a particle sedimenting in a static fluid and its terminal velocity, except that here the external force is imposed (rather than a result of gravity) and the granular bed flows with a uniform shear rate. Furthermore, we note that an intruder particle in a granular shear flow may experience shear-induced lift effects due to possible velocity differences (i.e., slip velocity) between the intruder and the nearby mean flow in the streamwise direction (van der Vaart *et al.* 2018). Therefore, the effective drag force F_d defined in this paper, similar to previous work (Tripathi & Khakhar 2011; Liu & McCarthy 2017; Duan *et al.* 2020; Bancroft & Johnson 2021), simply represents the net resistive force on the intruder in the z-direction and, although different mechanisms contribute to F_d, our focus is the relation between F_d and w_i for various simulation conditions.

Following this procedure, we first vary F_{ext} over four orders of magnitude to explore possible drag regimes and identify the transition from viscous-like to inertial-like regimes. Then, focusing on the viscous regime, we develop a general scaling law for the drag force based on a comprehensive parametric study for different combinations of flow conditions (P_0 and $\dot{\gamma}_0$, hence I) and intruder properties (R and R_ρ). In total, results for over 1000 simulations are reported for the drag study. Finally, an additional set of about 80 simulations with gravity ($g = 9.81$ m/s^2) are conducted to explore the ability of our drag model, together with a previous segregation force model (Jing *et al.* 2020), to predict the intruder velocity in gravity-driven size and density segregation.

3. Results

3.1. *Typical drag behaviours ($R = 1$ and $R_\rho = 1$)*

We first consider applying F_{ext} to five intruder particles having the same size and density as the bed particles ($R = 1$ and $R_\rho = 1$). The drag force (or, equivalently, the applied driving force F_{ext}) is nondimensionalized as $F_d/(P_0 d_i^2)$ since $P_0 d_i^2$ is the only intrinsic (contact) force scale in this dense, simple shear flow, where gravity is not present and the contact pressure dominates over the kinetic pressure. In figures 2(a–d), four widely-varying values of $F_d/(P_0 d_i^2) = \{0.05, 0.5, 5, 50\}$ are used to show examples of the intruder position in z vs. time t, which are nondimensionalized by the bed particle diameter d and the shear rate $\dot{\gamma}_0$, respectively. The flow inertial number is $I = 0.08$ ($P_0 = 1000$ Pa and $\dot{\gamma}_0 = 10\ \mathrm{s}^{-1}$). Note that $t = 0$ in figure 2 denotes the time when F_{ext} is first applied on the intruder, prior to which the flow and the intruder are at steady state (for $t < 0$, the intruder is allowed to move with the flow but is vertically constrained at its initial height by a virtual spring; see Jing *et al.* (2021)).

Figure 2(a) shows that when F_d is much smaller than the typical contact force magnitude ($F_d/(P_0 d_i^2) = 0.05$), the intruder vertical position exhibits significant fluctuations and, occasionally, the intruder lingers around a certain flow depth or even rises briefly before continuing its downward trajectory (see also supplementary movie 1). This intermittency of the downward intruder migration due to a very small driving force is somewhat reminiscent of the sub-yielding behaviour of granular drag (Zheng *et al.* 2018) and is likely a consequence of random particle collisions acting on the intruder. Nevertheless, an overall trend of downward intruder migration is observed in the measurement window of $10 \leqslant z/d \leqslant 20$ (shaded area in figure 2a) and, therefore, a mean velocity w_i can be calculated as detailed in §2.2 and discussed in the subsequent analysis. Figures 2(b–d) show the temporal evolution of the intruder vertical position for three larger drag forces, $F_d/(P_0 d_i^2) = \{0.5, 5, 50\}$, respectively, which exhibit qualitatively similar trends as in figure 2(a) but with increasingly smaller fluctuations. Note that the horizontal time scale decreases by a factor of ten as $F_d/(P_0 d_i^2)$ is increased by ten times, indicating a (linearly) increasing velocity with increasing $F_d/(P_0 d_i^2)$. The mean intruder acceleration in the observation window is negligible, as is evident for the cases in figures 2(b–d), for the full range of F_d that we explore, indicating that the particles around the intruder react to the intruder migration such that a local quasi-equilibrium occurs with F_{ext} balanced by F_d.

To further explore the interaction between the intruder and its surrounding particles for these four example simulations, we visualize the corresponding mean flow fields around the intruder (filled circles) in figures 2(e–h), which include the local packing density ϕ' (colored surface plots and white contours) and the relative flow velocity (arrows) $\mathbf{u}' = \mathbf{u} - \mathbf{u}_i$, where $\mathbf{u}$ and $\mathbf{u}_i$ are the flow and intruder velocity vectors, respectively. For each intruder, the surrounding flow fields are evaluated within a $10d \times 1d \times 10d$ cross section centred at the intruder position (x_i, y_i, z_i) with a local coordinate system $(x', y', z') = (x - x_i, y - y_i, z - z_i)$. In this sub-domain, particle positions and velocities are first mapped onto a set of $0.2d \times 1d \times 0.2d$ grids, then smoothed via a disk filter (radius of d) in the $x'z'$-plane, and finally averaged over all output frames in the observation window for all five intruders. As figure 2(e) shows, when the drag force is very small ($F_d/(P_0 d_i^2) = 0.05$), the flow around the intruder is dominated by the primary shear flow in x' with negligible relative velocities in z', and the disturbance of the intruder on the packing density of the surrounding particles is negligible, although the contours of ϕ' show an excluded volume effect that is symmetric about the intruder, as expected (Tripathi & Khakhar 2011). The flow pattern for $F_d/(P_0 d_i^2) = 0.5$ (figure 2f) is similar

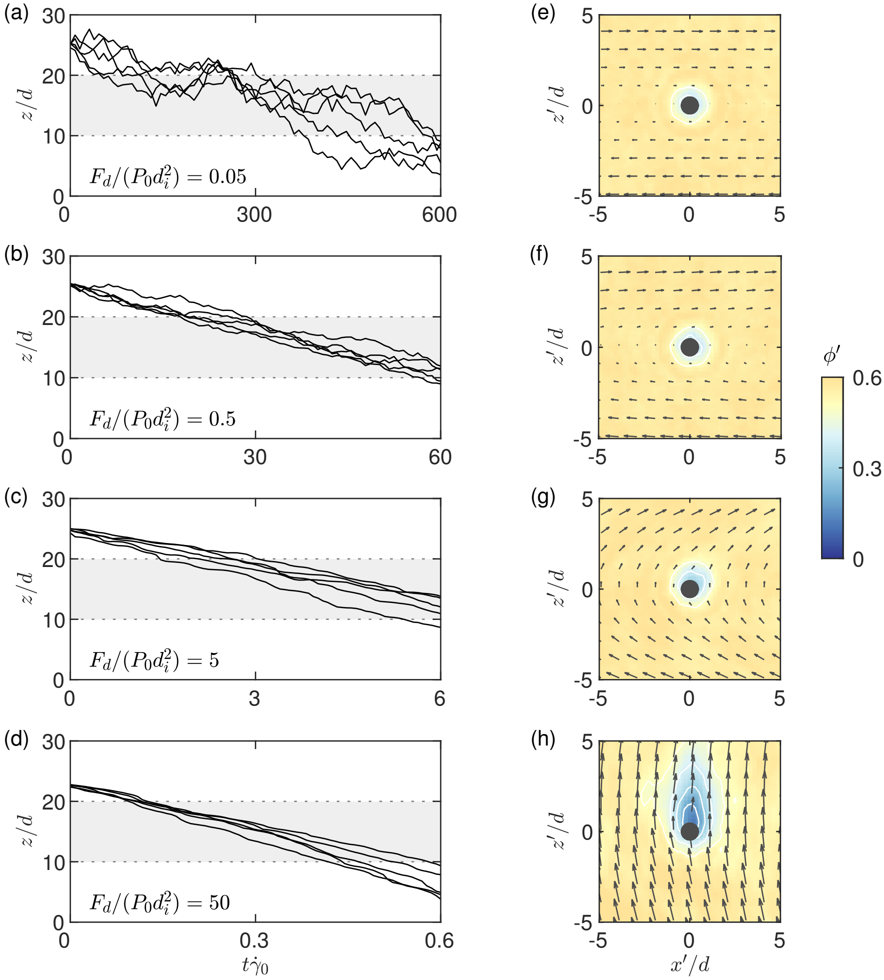

FIGURE 2. Examples of (a–d) intruder vertical position vs. time t and (e–h) corresponding flow fields around the intruder (in the intruder reference frame) for various drag forces F_d (see labels in the figure; note the differing horizontal time scales). The flow conditions are $P_0 = 1000$ Pa and $\dot{\gamma}_0 = 10$ s^{-1} ($I = 0.08$), and the intruder properties are $R = 1$ and $R_\rho = 1$. Grey areas in (a–d) indicate the measurement window where the intruder velocity (slope) and local flow fields are evaluated (see §2.2 and §3.1 for details). The white contours of local packing density ϕ' in (e–h) have an interval of 0.1 and the outermost contour is for $\phi' = 0.5$. For clarity, the velocity vectors are presented at a coarser resolution than the ϕ' fields and the arrows in (e–h) have different scales; the scale of w_i can be roughly inferred from figure 3 below.

to that for $F_d/(P_0 d_i^2) = 0.05$, but the velocity vectors display a small component in the z'-direction due to increasing relative velocity in z'. This becomes more evident when the drag force is increased to $F_d/(P_0 d_i^2) = 5$ (figure 2g), where the induced relative velocity in z' is approximately of the same order of that in x', and a semi-circular flow pattern is formed around the intruder, consistent with the shear flow relative to the intruder (rightward above the intruder and leftward below). Moreover, an asymmetric packing structure emerges with a decrease in the packing density (low ϕ' zone) above the intruder, essentially in the "wake" of the downward moving intruder (see also supplementary movie 2). Lastly, for the largest drag force, $F_d/(P_0 d_i^2) = 50$ (figure 2h), the relative velocity in z' dominates because the intruder velocity is much larger than the velocity associated

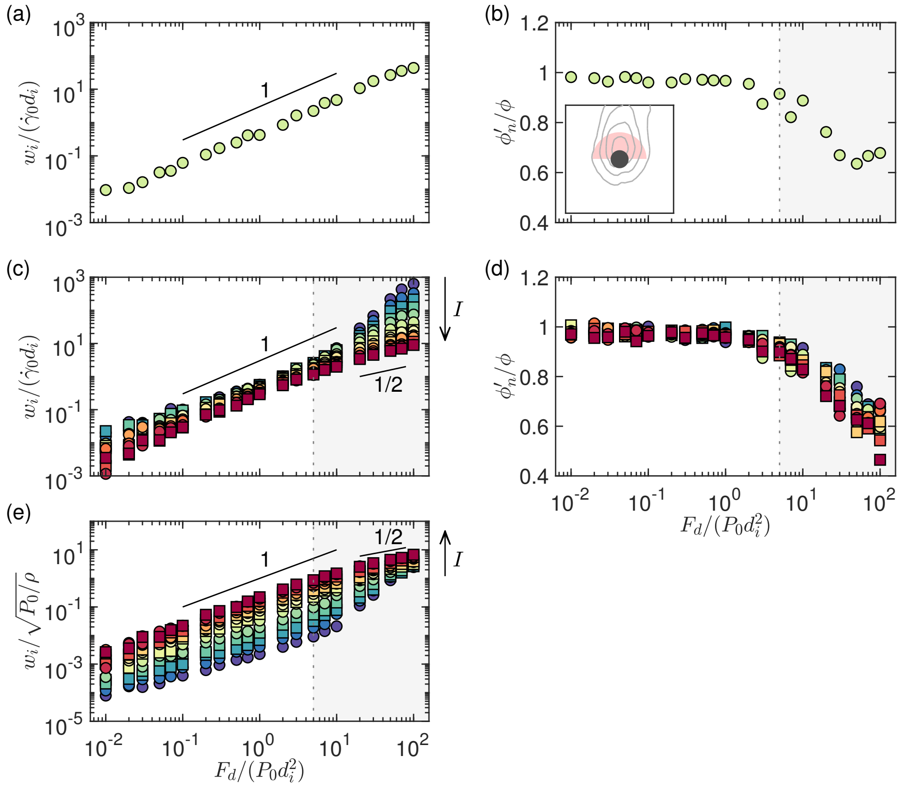

FIGURE 3. Drag force results for intruders equal in size and density to the surrounding bed particles ($R = 1$ and $R_\rho = 1$). (a) Intruder velocity $w_i/(\dot\gamma_0 d_i)$ and (b) nearby packing density ϕ'_n/ϕ vs. drag force $F_d/(P_0 d_i^2)$ for $P_0 = 1000$ Pa and $\dot\gamma_0 = 10$ s^{-1} ($I = 0.08$). The shaded red area in the inset of (b) indicates the region where ϕ'_n is evaluated. (c,d) are the same as (a,b) but for all flow conditions (same symbols as in figure 1). (e) Same as (c) except that w_i is non-dimensionalized by $\sqrt{P_0/\rho}$ instead of $\dot\gamma_0 d_i$. Grey shaded areas in (b–e) indicate the approximate conditions ($F_d/(P_0 d_i^2) \gtrsim 5$) where cavity formation is significant ($\phi'_n/\phi \lesssim 0.9$).

with the shear. In addition, a significant teardrop-shaped cavity (where ϕ' can be as low as zero) appears behind the intruder, indicating that the downward migration of the intruder is fast enough that the nearby particles cannot rearrange themselves quickly enough to refill the gap, resulting in a cavity behind the intruder. The significant changes in the local flow pattern and packing structure in figures 2(e–h) beg the question of how they might affect the scaling of F_d, which is described in the next subsection.

3.2. *Drag force regimes ($R = 1$ and $R_\rho = 1$)*

To characterize the regimes of the drag force, the intruder velocity $w_i/(\dot\gamma_0 d_i)$, averaged over five intruder particles for each condition, is plotted in figure 3 against the corresponding drag force $F_d/(P_0 d_i^2)$ for intruders having the same size and density as the surrounding particles ($R = 1$ and $R_\rho = 1$). The velocity is non-dimensionalized based on the shear time scale ($\dot\gamma_0$) and the intruder size (d_i), although non-dimensionalization using a velocity scale for the bed particle rearrangement ($\sqrt{P_0/\rho}$) is also considered.

Figure 3(a) presents the results of 21 simulations for varying $F_d/(P_0 d_i^2)$ that have the same flow conditions as those in figure 2, i.e., $I = 0.08$ ($P_0 = 1000$ Pa and $\dot\gamma_0 = 10$ s^{-1}). A linear relationship between $w_i/(\dot\gamma_0 d_i)$ and $F_d/(P_0 d_i^2)$ (i.e., a viscous-like regime) is found over a wide range of intermediate $F_d/(P_0 d_i^2)$ values. For very small forces, $F_d/(P_0 d_i^2) = \mathcal{O}(10^{-2})$, scatter of the data increases (error bars are not shown as they are generally smaller than the symbols) due to increased fluctuations and intermittency in the temporal evolution of the intruder vertical position, as shown in figure 2(a). For very large forces, $F_d/(P_0 d_i^2) = \mathcal{O}(10)$, the slope of the curve deviates slightly from one, which we attribute to the inertial effect of cavity formation as shown in figure 2(h). Furthermore, to quantitatively identify the transition between the viscous and inertial regimes, we plot a local packing density in the wake of the intruder ϕ_n'/ϕ against $F_d/(P_0 d_i^2)$ in figure 3(b), which starts to drop significantly below one when $F_d/(P_0 d_i^2)$ exceeds about 5 due to cavity formation. Here, ϕ_n' is the mean value of ϕ' within a nearby semi-circular annular region located above the intruder having an arbitrary outer radius $1.5d_i$ from the centre of the intruder, as illustrated in the inset of figure 3(b), and the normalization of ϕ_n'/ϕ eliminates the influence of I on the average packing density ϕ (see figure 1c).

Figures 3(c,d) show the results of 315 simulations ($R = 1$ and $R_\rho = 1$) for all the flow conditions that we explore (characterized by I), where the symbol colours and shapes match those in figures 1(b,c). Several key observations can be made. First, the transitional behaviours related to intermittent intruder migration at the low end and cavity formation at the high end for the curves in figure 3(c) are similar despite the wide range of I (from 0.004 to 0.75). In particular, all curves are linear (slope one) in an intermediate range of $F_d/(P_0 d_i^2)$, approximately between 0.1 and 5, indicating a viscous scaling for the drag force, $F_d/(P_0 d_i^2) \propto w_i/(\dot\gamma_0 d_i)$, or $F_d \propto (P_0/\dot\gamma_0) d_i w_i$, which corresponds to the example intruder dynamics in figures 2(b,c). Outside this viscous-like regime, data scatter grows for $F_d/(P_0 d_i^2) \lesssim 0.1$, making it hard to accurately characterize the F_d vs. w_i relation due to the increasing fluctuations and intermittency of the intruder migration (figure 2a), and a change of slope occurs for $F_d/(P_0 d_i^2) \gtrsim 5$ due to inertial effects such as the cavity formation in figure 2(h). Second, in the inertial regime ($F_d/(P_0 d_i^2) \gtrsim 5$), the slopes of the curves show non-trivial dependence on I, which is clarified below with respect to figure 3(e); nevertheless, it is evident that the curves for high inertial numbers (red symbols) approach a slope of 1/2, indicating the familiar quadratic scaling $F_d \propto w_i^2$ for inertial drag of collisional granular flows (Jenkins & Yoon 2002; Seguin & Gondret 2017; Das *et al.* 2020). Finally, as a signature of the transition from the viscous regime to the inertial regime, significant cavity formation occurs in the wake of the intruder when $F_d/(P_0 d_i^2) \gtrsim 5$, regardless of I (i.e., rapid drop of ϕ_n'/ϕ in figure 3d), which suggests a threshold value beyond which the contact forces that drive particle rearrangement (which scale with $P_0 d^2$) are inadequate to quickly fill the wake behind the intruder.

The diverging slopes of the curves for $F_d/(P_0 d_i^2) \gtrsim 5$ in figure 3(c) are a result of the chosen velocity scale, $w_i/(\dot\gamma_0 d_i)$. Indeed, w_i is expected to be independent of $\dot\gamma_0$ in the inertial regime, where the intruder transits downward so rapidly that the shear is negligible in the intruder reference frame; see figure 2(h). Instead, a relevant velocity scale that determines how fast the bed particles rearrange near the intruder is $\sqrt{P_0/\rho}$. Figure 3(e) shows the rescaled intruder velocity $w_i/\sqrt{P_0/\rho}$ vs. $F_d/(P_0 d_i^2)$, indicating a clear convergence of all curves to the highest-I curve and toward the same slope of 1/2 in the inertial regime (shaded area). This leads to an inertial drag force scaling of $F_d/(P_0 d_i^2) \propto (w_i/\sqrt{P_0/\rho})^2$, or $F_d \propto \rho d_i^2 w_i^2$. Interestingly, the transition of the slope from one to 1/2 is more direct for high-I cases (red symbols) than low-I cases (blue symbols), perhaps because when I is low ($I \lesssim 0.01$), where the bed deformation is otherwise quasi-static (Azéma & Radjaï 2014), the intruder needs to sufficiently fluidize the nearby bed particles such that its migration behaviour transitions from the viscous to inertial regimes. Another interesting observation in figure 3(e) is that the curves do not collapse

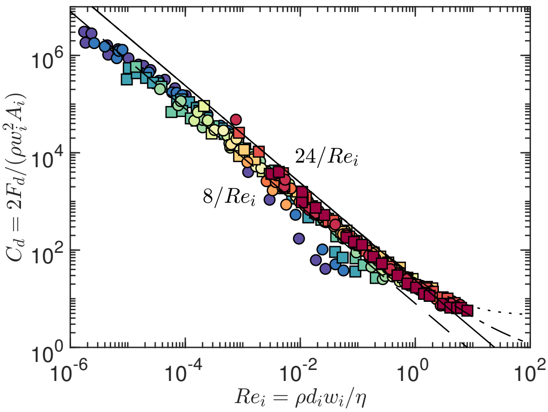

FIGURE 4. Drag coefficient C_d vs. intruder Reynolds number Re_i for $R = 1$ and $R_\rho = 1$. Data are recast from figure 3(c) with the same symbols. The solid, dashed, dotted, and dot-dash curves represent relations $C_d = 24/Re_i$, $C_d = 8/Re_i$, $C_d = 24/Re_i(1 + 3Re_i/16)$, and $C_d = 24/Re_i + 6/(1 + \sqrt{Re_i}) + 0.4$, respectively (see text).

in the viscous regime ($F_d/(P_0 d_i^2) \lesssim 5$) when w_i is scaled by $\sqrt{P_0/\rho}$, in contrast to the data collapse in figure 3(c) where w_i is scaled by $\dot\gamma_0 d_i$. This justifies our choice of the dimensionless velocity $w_i/(\dot\gamma_0 d_i)$ throughout this paper, since the intruder drag is mainly in the viscous-like regime.

3.3. *Viscous-like drag force scaling ($R = 1$ and $R_\rho = 1$)*

The results in figure 3 show that the drag force follows a viscous-like scaling ($F_d \propto w_i$) over a wide range of $F_d/(P_0 d_i^2)$, which is reminiscent of the Stokes regime for the drag of a sphere in a uniform flow of a viscous fluid. To demonstrate this analogy more quantitatively, we recast the data in figure 3(c) as the drag coefficient, C_d, vs. the intruder Reynolds number, Re_i, in figure 4, as is often done for the drag on a sphere in a fluid. Here, $C_d = 2F_d/(\rho w_i^2 A_i)$, $A_i = \pi d_i^2/4$, $Re_i = \rho d_i w_i/\eta$, and $\eta = \mu P_0/\dot\gamma_0$ is the effective granular flow viscosity with $\mu = \mu(I)$ described by the curve in figure 1(b). The data fall onto a master curve with a slope of -1 in figure 4. The viscous relation $C_d \propto 1/Re_i$ extends over a surprisingly wide range of Re_i from 10^{-5} to 1. Deviations from this viscous relation occur for $Re_i < 10^{-5}$ and $Re_i > 1$, respectively, due to the fluctuation- and inertia-related effects discussed above; only a few data points (bluish data points below the dashed line) deviate from the master curve due to the transitional behaviour from slope one to slope 1/2 for low-I cases ($I \lesssim 0.01$), as discussed above regarding figure 3(e).

In figure 4, we further indicate the $C_d = 24/Re_i$ (total drag; solid curve) and $C_d = 8/Re_i$ (form drag; dashed curve) relations (see, e.g., White 1974) to directly compare our "granular drag" data with Stokes' viscous drag for a sphere. Our data falls between these two limiting cases, indicating a form for the granular drag coefficient, $C_d = 8c/Re_i$, where c is a prefactor ranging approximately from 1 to 3 (i.e., bounded by the dashed and solid curves). Alternatively, this is rewritten as a Stokes-like drag force,

$$F_d = c\pi\eta d_i w_i, \tag{3.1}$$

where the prefactor c depends somewhat on simulation conditions (see §3.4). Note that, as mentioned in §2.2, the signs of F_d and w_i are omitted for brevity, although F_d is opposite to w_i. Expression (3.1) is precisely the Stokes drag model for a sphere in a viscous fluid if $c = c_{St}$, where $c_{St} = 3$ is the sum of the form drag ($c_{St}/3$) and the friction drag ($2c_{St}/3$) (White 1974). Although we make no claim of a direct analogy, it is interesting that the prefactor c in a dense granular flow varies from $c_{St}/3 = 1$ (form drag) to $c_{St} = 3$ (total drag), which highlights the subtle differences between dissipation due to particle interactions in a granular flow and that due to viscosity in a fluid. Moreover, we have verified that the DEM contact parameters do not affect the C_d vs. Re_i results (as noted in §2.1), consistent with previous results (Tripathi & Khakhar 2011; Bancroft & Johnson 2021). This further indicates that granular drag is the collective consequence of particle interactions typical of dense granular flows.

Finally, it is also interesting to note that, for $Re_i > 1$, the data tends to level off with increasing Re_i, similar to the non-Stokesian drag behaviour of a sphere in a fluid due to inertia-related effects (Goossens 2019, and references therein). To further demonstrate this, in figure 4, we plot both Oseen's drag model (Schlichting 1979), $C_d = 24/Re_i(1 + 3Re_i/16)$, which is strictly valid only for $Re_i < 5$ (dotted curve), and the empirical fit by White (White 1974), $C_d = 24/Re_i + 6/(1 + \sqrt{Re_i}) + 0.4$ (dot-dash curve). Both relations suggest that the similarity between the drag on a spherical particle in a granular flow and the drag on a sphere in a fluid extends beyond the viscous Stokes flow regime ($Re_i \lesssim 1$) into the inertial flow regime.

We caution here that the analogy with drag on a sphere in a fluid is imperfect. For a sphere in a fluid, the drag force is based on moving the sphere through a quiescent fluid (or, equivalently, a uniform fluid flow over a stationary sphere). As a result, there is no lift force. The situation differs here in that the spherical intruder particle is moved through a sheared granular medium (i.e., transiting through regions with decreasing mean flow velocities) so that we can connect these drag results to those for segregating particles in sheared granular flows, as in previous work on this topic (Tripathi & Khakhar 2011; Liu & McCarthy 2017). However, the uniform shear velocity field may lead to lift forces when there is a slip velocity between the intruder and the sheared bed. Hence, the drag force we measure is essentially the "net resistive drag force," which may include effects related to the effective streamwise slip of the intruder relative to the shear flow, as discussed later in this paper.

3.4. *Drag force for varying R and R_ρ*

To investigate the effects of the intruder size ratio $R = d_i/d$ and density ratio $R_\rho = \rho_i/\rho$ on the drag force, we vary d_i and ρ_i, respectively, for various I. Figure 5 presents two representative scenarios with $R = 4$ and $R_\rho = 1$ (blue symbols) and with $R = 1$ and $R_\rho = 10$ (red symbols), where the degree of colour saturation from light to dark indicates the three values of $I = \{0.004, 0.16, 0.64\}$; the results from figure 3 (with $R = 1$ and $R_\rho = 1$) are reproduced as grey crosses in figure 5 for comparison. As figure 5(a) shows, when $R = 4$, the basic drag characteristics (linear and nonlinear regimes) for various I are similar to those for $R = 1$, but the curves are shifted downward, indicating that a larger drag force is needed to achieve the same intruder velocity. The shift is the consequence of a stronger disturbance in the flow as the larger intruder transits through the flow, which is evident in the larger low-density area around the intruder in the inset of figure 5(b) (see also supplementary movie 3). Interestingly, the transition of ϕ'_n/ϕ for $R = 4$ is similar to that for $R = 1$ (see figure 5b), indicating that under the same $F_d/(P_0 d_i^2)$ the cavity shape is similar for different R, although the cavity size scales approximately with the cross-sectional area of the intruder. Moreover, the effect of R on the F_d vs. w_i scaling (figure 5a) is even smaller than that on the near-intruder flow density (figure 5b), indicating again that the intruder drag originates mainly from particle interactions at its leading edge but is less affected by the cavity area in its wake. Perhaps more important is that the

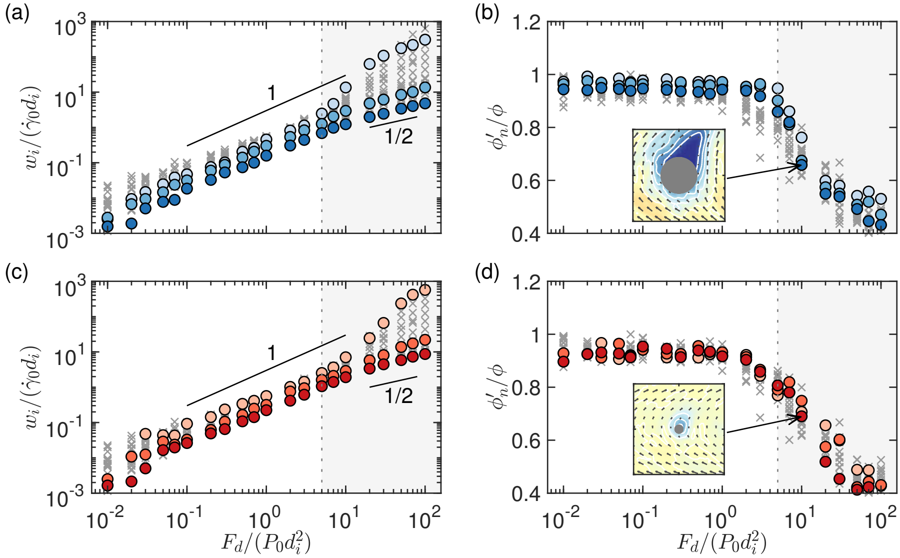

FIGURE 5. Effects of larger size ratio ($R = 4$ and $R_\rho = 1$, blue symbols, upper panels) and larger density ratio ($R = 1$ and $R_\rho = 10$, red symbols, lower panels) on (a,c) $w_i/(\dot{\gamma}_0 d_i)$ vs. $F_d/(P_0 d_i^2)$ and (b,d) ϕ_n'/ϕ vs. $F_d/(P_0 d_i^2)$ results. Light, medium, and dark colours correspond to $I = \{0.004, 0.16, 0.64\}$, respectively, and grey crosses are $R = 1$ and $R_\rho = 1$ data reproduced from figures 3(b,d) for comparison. Insets in (b,d) at $F_d/(P_0 d_i^2) = 10$ and $I = 0.64$ demonstrate the near-intruder flow fields using the same colour map as figures 2(e–h). Grey shaded areas match those in figures 3(b–e).

$w_i/(\dot{\gamma}_0 d_i)$ vs. $F_d/(P_0 d_i^2)$ relation remains linear in the same range of $F_d/(P_0 d_i^2)$ as for $R = 1$, and that, although not shown, the $w_i/\sqrt{P_0/\rho}$ vs. $F_d/(P_0 d_i^2)$ relation transitions toward slope 1/2 for large $F_d/(P_0 d_i^2)$, similar to the $R = 1$ results in figure 3(e).

The results for $R_\rho = 10$ show that the influence of the intruder density on the $w_i/(\dot{\gamma}_0 d_i)$ vs. $F_d/(P_0 d_i^2)$ relation (figure 5c) and the flow field around the intruder (figure 5d) are less significant than the intruder size effects at $R = 4$, although a slightly lower intruder velocity is observed for large $F_d/(P_0 d_i^2)$ cases in the more collisional flow ($I = 0.64$), indicating a slightly larger drag force (figure 5c). The effects of R and R_ρ on the drag force is discussed in greater detail in §3.5.

Figure 6 shows that recasting the data in figures 5(a,c) into the C_d vs. Re_i form leads to results that remain bounded by the $8/Re_i$ and $24/Re_i$ scaling, except for a few cases related to the transitional behaviour of low-I cases (similar to figure 4). Therefore, as a first-order approximation, the drag force on a spherical particle ($1 \leqslant R \leqslant 4$ with $R_\rho = 1$ and $1 \leqslant R_\rho \leqslant 10$ with $R = 1$) in a dense granular flow ($10^{-3} \lesssim I \lesssim 1$) can be estimated by a Stokesian drag coefficient $C_d = 8c/Re_i$, where c ranges approximately from 1 to 3, for a wide range of intruder Reynolds numbers ($10^{-5} \lesssim Re_i \lesssim 1$). For larger Reynolds numbers ($1 \lesssim Re_i \lesssim 100$), the data indicate that C_d deviates from this relation due to inertial effects, following the Oseen approximation for $R_\rho = 10$ and the White empirical fit for $R = 4$ (figure 6). While this result is interesting, we do not explore it further in this paper.

3.5. *Dependence of drag prefactor c on parameters*

Despite the data collapse to a master curve $C_d = 8c/Re_i$ in figures 4 and 6, it is evident that the prefactor c exhibits (secondary) dependence on the flow condition (I) and the intruder properties (R and R_ρ), i.e., $c = c(I, R, R_\rho)$. To further examine this dependence,

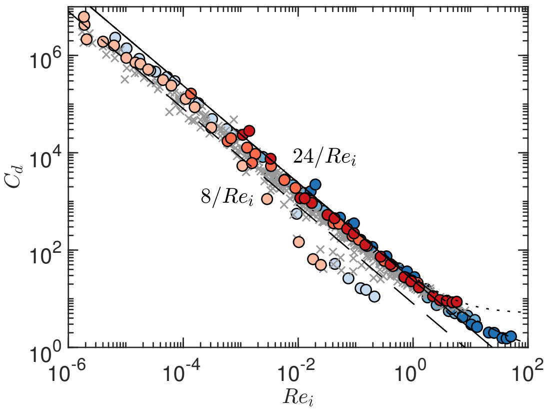

FIGURE 6. Results for $R = 4$ (blue symbols) and $R_\rho = 10$ (red symbols) in terms of C_d vs. Re_i; data recast from figures 5(a,c). Grey crosses are reproduced from figure 4 for reference, while the solid, dashed, dotted, and dot-dash curves are the same as those in figure 4.

we use the drag force expression (3.1) to obtain the mean value of $c = F_d/(\pi\eta d_i w_i)$ for a given set of (I, R, R_ρ) conditions; see figure 7. Note that, to focus on the linear regime ($F_d \propto w_i$), we only consider the F_d vs. w_i data associated with $0.1 \leqslant F_d/(P_0 d_i^2) \leqslant 5$ according to the discussion with respect to figure 3. Each value for c plotted in figure 7 represents an average over six to nine simulations (in total, about 800 simulations); unaveraged data can be found in figure 9 (which includes all simulation conditions) and figure 11(a) in Appendix C (which only includes simulations with $0.1 \leqslant F_d/(P_0 d_i^2) \leqslant 5$).

Figure 7(a) presents the dependence of c on I for $R = 1$ (dark grey symbols) and $R = 4$ (light grey symbols) (keeping $R_\rho = 1$) and shows that c increases linearly with I with a slope that is steeper for $R = 4$ than for $R = 1$. Interestingly, for $R = 1$, c only varies slightly, from 1.45 to 1.75, for the full range of I that we consider, which agrees with our previous result ($c \approx 1.73$ regardless of I; dotted horizontal line in figure 7a) for density-bidisperse mixtures (rather than isolated intruder particles) with a volume concentration varying from 0.3 to 0.7 (Duan *et al.* 2020).

Figure 7(b) shows the dependence of c on R for $I = \{0.008, 0.16, 0.32, 0.64\}$, where R is varied from 0.6 to 5 with an increment of 0.2 (keeping $R_\rho = 1$). A self-similar behaviour is observed for each I, where c first increases sharply for small R and then increases more gradually with a slope that depends on I. The crossover of these two regimes in the range $1 \lesssim R \lesssim 2$ suggests a geometric effect, likely because an intruder particle with $R > 1$ has a greater impact on the nearby flow field (see figure 5b inset) than a smaller intruder ($R \lesssim 1$) that can more easily pass through voids. The linear increase of c with increasing R above this range indicates an inertial effect related to the intruder size ratio (hence the mass ratio), which is stronger when I is increased toward more collisional flows (Liu & McCarthy 2017). The inertial effect could also be related to a lift force induced by a slip velocity between the intruder and the mean flow in the streamwise direction (Ding *et al.* 2011; van der Vaart *et al.* 2018), which is expected to be more significant for greater R, because a larger, and hence heavier, intruder has more inertia thereby increasing the likelihood of a greater slip velocity. However, a more precise consideration of a possible lift-like force is beyond the scope of this work.

Figure 7(c) presents the dependence of c on R_ρ for $I = \{0.008, 0.16, 0.32, 0.64\}$, where R_ρ is varied from 1 to 20 (keeping $R = 1$). Similar to figure 7(b) for R, c increases linearly with R_ρ and the effect is stronger for greater I, which can also be attributed to mass-ratio effects at particle collisions (Liu & McCarthy 2017) and lift effects due to possible

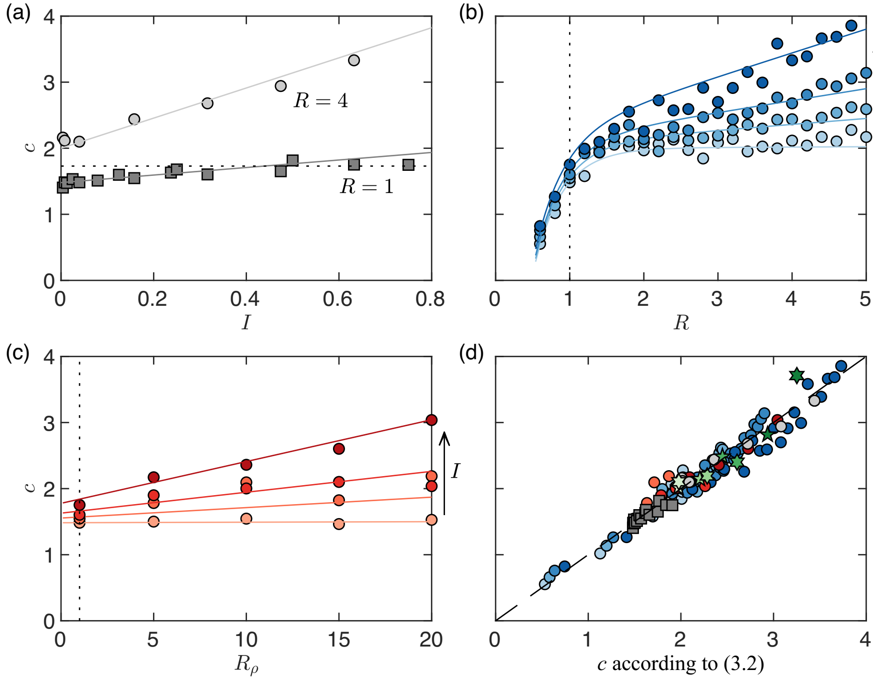

FIGURE 7. Dependence of c on I, R and R_ρ. (a) c vs. I (with $R_\rho = 1$) for $R = 1$ (squares) and $R = 4$ (circles). The dotted line indicates a previous result of $c = 1.73$ for $R = 1$ (Duan *et al.* 2020). (b) c vs. R (with $R_\rho = 1$) and (c) c vs. R_ρ (with $R = 1$) for $I = \{0.008, 0.16, 0.32, 0.64\}$, where symbols with light to dark shading indicate increasing I and the dotted vertical lines indicate $R = 1$ and $R_\rho = 1$, respectively. In (a–c), the solid curves with colours matching the corresponding symbols are based on the empirical fit (3.2), which is developed in Appendix B. (d) Measured value of c from simulations vs. c according to (3.2) for all conditions in (a–c) and additional conditions of $(R, R_\rho) = (2, 5)$ and $(R, R_\rho) = (2, 10)$ for $I = \{0.008, 0.16, 0.32, 0.64\}$ (green symbols). The dashed diagonal line indicates perfect prediction.

slip velocities, as discussed above. Note that the dependence of c on R_ρ is negligible for $I = 0.008$, where such inertial effects are expected to be insignificant when the flow is close to quasistatic. However, although the effects of R_ρ on c appear to be similar to the effects of R, plotting c against the intruder mass ratio ($R_m = R^3 R_\rho$) does not collapse the data in figures 7(b,c) due to the non-trivial geometric effect on the drag for $R \lesssim 1.5$ in figure 7(b).

To investigate whether the individual effects of R and R_ρ on c are additive for different I, we empirically fit the data in figures 7(a–c) to a function,

$$c = [k_1 - k_2 \exp(-k_3 R)] + s_1 I R + s_2 I (R_\rho - 1), \tag{3.2}$$

which is motivated by a form for a viscoplastic constitutive relation having an appearance similar to that for the data in figure 7(b) and assumes additivity between the R- and R_ρ-related terms (see Appendix B for details). The values for c based on this ad hoc approach are compared in figure 7(d) with the measured c from various simulations, showing good agreement for simulations where R and R_ρ are varied individually (red and blue circles) and two additional sets of simulations (green stars) with intruder properties $(R, R_\rho) = (2, 5)$ and $(R, R_\rho) = (2, 10)$ for various inertial numbers ($I = \{0.008, 0.16, 0.32, 0.64\}$). The good agreement indicates that mass effects due to intruder size and density ratios are indeed additive, at least to a first approximation for the conditions tested here ($0.6 \leqslant R \leqslant$

5, $1 \leqslant R_\rho \leqslant 20$, and $I \lesssim 1$). However, as a caveat, we note that if R and R_ρ are varied too far beyond the aforementioned conditions (which, e.g., we observe for extreme conditions of $R = 4$ and $R_\rho = 4$ or $R = 1$ and $R_\rho = 256$, both yielding $R_m = 256$), the empirical relation (3.2) can become inapplicable, and the near-intruder flow fields exhibit patterns very different from those in figures 2 and 5. Nevertheless, these extreme behaviours are not observed in any simulations reported elsewhere in this paper ($R_m \leqslant 125$).

To summarize the results in figure 7, c generally increases with increasing I, R, and R_ρ, ranging approximately between 1 and 3 (corresponding to the $C_d = 8/Re_i$ and $C_d = 24/Re_i$ lines in figures 4 and 6) except for a few cases with $R = 0.6$ or $I = 0.64$. The value of c can be described approximately by an ad hoc empirical relation (3.2), which is reasonably effective for R and R_ρ varied individually or together.

4. Discussion

4.1. *Connections of the drag model with previous work*

We have shown that in the viscous regime ($0.1 \leqslant F_d/(P_0 d_i^2) \leqslant 5$), the drag force dependence on the intruder velocity can be expressed as a modified Stokes law, $F_d = c(I, R, R_\rho)\pi\eta d_i w_i$, where $\eta = \mu(I)P_0/\dot{\gamma}_0$ encapsulates the influence of flow conditions, for a broad (I, R, R_ρ) parameter space. Previous work on the drag in granular flows addressed the drag force on individual heavy intruders in otherwise monodisperse flows (Tripathi & Khakhar 2011; Liu & McCarthy 2017) or the drag in sheared density-bidisperse mixtures with a narrower range of size-bidispersity (Duan *et al.* 2020; Bancroft & Johnson 2021), leading to several different drag models. Here, we discuss three aspects of the connections between our results and previous work.

First, as noted with respect to figure 7(a), the parameter c that we obtain for $R = 1$ ($1.45 < c < 1.75$) agrees quantitatively with the result ($c \approx 1.73$) of our recent work (Duan *et al.* 2020), where the drag force is measured in density-bidisperse (i.e., $R = 1$) uniform shear flows with various particle concentrations. Similarly, Bancroft & Johnson (2021) also report insensitivity of their drag coefficient to the particle concentration in uniform shear flows. The similarity of c between intruder (this work) and mixture regimes (Duan *et al.* 2020; Bancroft & Johnson 2021), at least for $R = 1$, suggests interesting future directions to elucidate the concentration dependence of the drag force in size- and density-bidisperse mixtures and extend the current findings toward more general drag models analogous to recent results for force partitioning that can be applied in continuum segregation theories (Duan *et al.* 2022).

Second, we have shown that an effective viscosity η can account for dissipation effects in granular flows in analogue to the drag in a viscous fluid, which leads to the Stokesian drag model of equation (3.1). The same viscosity-based approach is used in Tripathi & Khakhar (2011) and Duan *et al.* (2020). Alternatively, other studies (Liu & McCarthy 2017; Duan *et al.* 2020; Bancroft & Johnson 2021) consider the drag in terms of collisional effects in granular flows based on kinetic theory arguments (Jenkins & Yoon 2002). In particular, Bancroft & Johnson (2021) show that the strength of the drag force scales as $I^{-7/4}$ without an explicit consideration of the effective viscosity η. Interestingly, as detailed in Appendix C, our drag model can be recast into an $I^{-7/4}$ form, and the resulting scaling is slightly more general than that of Bancroft & Johnson (2021) as it captures the results for the full range of I, R, and R_ρ.

Finally, our results for the drag force using uniform shear to avoid gradient-induced segregation forces are quantitatively consistent with other work using uniform shear (Liu & McCarthy 2017; Duan *et al.* 2020; Bancroft & Johnson 2021). However, the dependence of c on I for $R = 1$ ($1.45 < c < 1.75$; figure 7a) only agrees qualitatively with studies using inclined chute flow (Tripathi & Khakhar 2011, 2013), where c increases from 2.57 to 3.67 as the chute slope is increased from 22° to 29° (for $R = 1$). Our preliminary investigation attributes this discrepancy to an interesting effect related to the direction of the external forcing: in uniform shear flows (no gravity) the external force F_{ext} is applied perpendicular to the shear direction (figure 1a), while in inclined chute flows the external force (due to gravity) has a component parallel to the shear flow. Indeed, when we tilt F_{ext} toward the positive x-direction, a greater drag coefficient is measured in the z-direction (data not shown). We speculate that the drag enhancing effect is related to a lift force (in z) on the intruder particle as the x-component of F_{ext} induces a velocity difference between the intruder and the mean flow in the x-direction (Ding *et al.* 2011; van der Vaart *et al.* 2018; van Schrojenstein Lantman 2019; van Schrojenstein Lantman *et al.* 2021). Further investigation is warranted to address this issue more conclusively but is beyond the scope of this work.

4.2. *Implications for gravity-driven segregation*

An important application of the results obtained in this paper is in models of mixing and segregation, for which a central question is how to connect the segregation velocity (or flux) with flow conditions (Umbanhowar *et al.* 2019). In the single intruder limit considered here, this can be done by resolving the segregation velocity based on the equation of motion of the intruder particle, provided that all relevant forces acting on the intruder are known. In a more typical granular flow where gravity is present, the forces acting on the intruder include the intruder weight, the segregation driving force F_{seg} (Guillard *et al.* 2016; van der Vaart *et al.* 2018; Jing *et al.* 2021), and the net resistive drag force F_d, noting that both F_{seg} and F_d originate from particle contacts and the net contact force on the intruder is not necessarily aligned with the shear, e.g., in inclined-plane flows (Tripathi & Khakhar 2011; Jing *et al.* 2017; van Schrojenstein Lantman 2019; van Schrojenstein Lantman *et al.* 2021). For simplicity, we consider a horizontal shear flow in the x-direction where gravity is in the negative z-direction, and focus only on the vertical motion of the intruder relative to the bed; that is, along the z-direction,

$$m_i \frac{\partial w_i}{\partial t} = -m_i g + F_{seg} + F_d, \tag{4.1}$$

where $m_i = (\pi/6)\rho_i d_i^3$ is the intruder mass, g is the gravitational acceleration, and $F_d = -c\pi\eta d_i w_i$ is the viscous drag force established here (note that the signs of F_d and w_i have been omitted up to this point but are now specified for clarity). As is evident from (4.1), the segregation propensity (rising and sinking) of the intruder particle in the z-direction depends only on the imbalance between $m_i g$ and F_{seg} (Jing *et al.* 2020), while the intruder velocity w_i depends further on the net resistive drag force F_d.

Generally, the segregation force F_{seg} consists of two additive terms related to pressure gradients and shear gradients along the z-direction in the flow (Guillard *et al.* 2016; Jing *et al.* 2021). To further simplify the problem, we consider a uniform shear flow in the presence of gravity (which is possible using the stabilizing force approach as detailed in Appendix A), where F_{seg} is well described by a size-ratio-dependent buoyancy force (Jing *et al.* 2020), i.e., $F_{seg} = f\phi\rho g V_i$. Here, $f = f(R)$ is a dimensionless empirical function independent of I (Jing *et al.* 2020) and is reproduced as the dotted curve in figure 8(a), $\phi\rho$ represents the bulk density of the granular flow, and $V_i = (\pi/6)d_i^3$ is the intruder volume. Assuming steady-state intruder migration ($\partial w_i/\partial t = 0$) in the z-direction, which

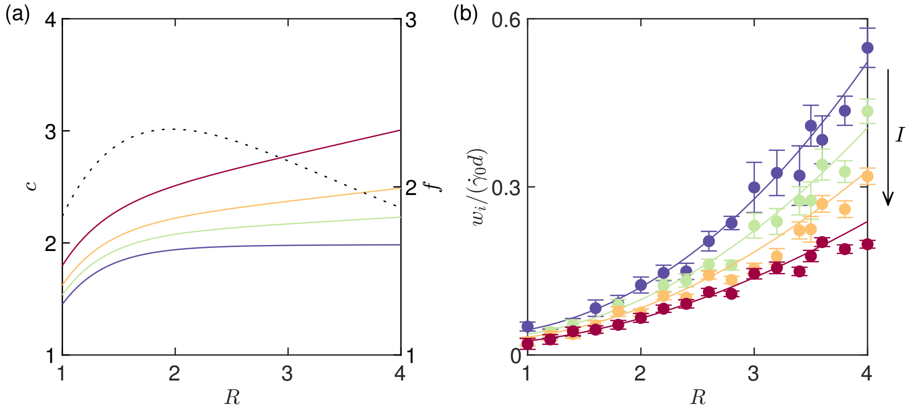

FIGURE 8. (a) Solid curves (left axis) are $c = c(R)$ for $R_\rho = 4$ and $I_{loc} = \{0.005, 0.1, 0.2, 0.4\}$ (see text) according to the empirical fit (3.2); colours from blue to red indicate increasing I. The dotted curve (right axis) is $f(R) = [1 - 1.43\exp(-R/0.92)][1 + 3.55\exp(-R/2.94)]$, which is independent of I (Jing *et al.* 2020). (b) Simulation results of $w_i/(\dot{\gamma}_0 d)$ vs. R (circles) for gravity-induced sedimentation of heavy intruders in uniform shear flows (see text) and the corresponding predictions (curves) of model (4.2); colours from blue to red match those in (a). Error bars in (b) represent the standard error of w_i.

is typical for intruders in dense granular flows (Staron 2018), and substituting the force models above into (4.1) leads to an expression for the intruder velocity,

$$w_i = -\frac{(\rho_i - f\phi\rho)gd_i^2}{6c\eta}, \tag{4.2}$$

which is similar to the terminal velocity of a sphere in a viscous fluid (i.e, if $f = 1$ and $c = 3$), but with modified buoyancy and drag terms, i.e., $f = f(R)$ and $c = c(I, R, R_\rho)$, to account for granular effects. Note that w_i is negative if $\rho_i > f\phi\rho$ (i.e., the intruder sinks) and is positive if $\rho_i < f\phi\rho$ (i.e., the intruder rises), keeping in mind that the negative sign for w_i due to the downward applied F_{ext} has been omitted in the plots throughout this paper. The previously known effects of the (local) pressure (P) and shear rate ($\dot{\gamma}$) on the segregation velocity (Fry *et al.* 2018; Trewhela *et al.* 2021) are captured in equation (4.2) by the (local) effective viscosity, $\eta = \mu(I)P/\dot{\gamma}$, although c also depends on I (figure 7). In particular, the form of our segregation velocity expression (4.2), after substituting in the expression for η, resembles a recent experimental scaling law for the intruder velocity in cyclic shear (Trewhela *et al.* 2021), $w_i \propto \mathcal{F}(R)\rho g\dot{\gamma}d^2/(\mathcal{C}\rho g d + P)$, where $\mathcal{F}(R)$ and $\mathcal{C}$ are empirical fits, which is based on velocity measurements and dimensional analysis.

To test (4.2) for its applicability to gravity-driven segregation of intruder particles, we run additional simulations with the same setup as figure 1(a), except with $g = 9.81$ m/s^2 in the vertical direction and $F_{ext} = 0$, allowing heavy intruders (with a fixed density ratio of $R_\rho = 4$ and various R from 1 to 4) to sink under gravity through the flow with four sets of flow conditions ($P_0 = 1000$ Pa and $\dot{\gamma}_0 = \{1, 20, 40, 80\}$ s^{-1}). In each simulation, a constant shear rate $\dot{\gamma}_0$ is maintained due to the stabilizing forces (Appendix A), but the stress fields are no longer homogeneous as gravity introduces a constant vertical pressure gradient. Therefore, instead of using system parameters P_0 and $\dot{\gamma}_0$, we measure the average values of ϕ, μ, P, and $\dot{\gamma}$ (as well as the corresponding mean intruder velocity w_i) over a 10d-thick layer in the middle of the flow to compute the local inertial number $I_{loc} = \dot{\gamma}d/\sqrt{P/\rho}$ and viscosity $\eta = \mu P/\dot{\gamma}$; note that these local measurements are undisturbed by the presence of intruders due to spatial smoothing and temporal averaging (Jing *et al.* 2021). The simulation results for w_i vs. R for each set of flow conditions ($I_{loc} = \{0.005, 0.1, 0.2, 0.4\}$, respectively) are presented as symbols (from blue to red colours) in figure 8(b). Note that w_i is normalized by $\dot{\gamma}_0 d$, a constant characteristic velocity for each data series. Interestingly, the values of $w_i/(\dot{\gamma}_0 d)$ (varying from 0.01 to 0.3) for $R \lesssim 3$ are quantitatively consistent with previous segregation velocity results for size-bidisperse and density-bidisperse mixtures in heap flows (Schlick *et al.* 2015; Xiao *et al.* 2016; Duan *et al.* 2021), confirming the connection between w_i determined from the force balance on a single intruder (4.2) and the segregation velocity model determined in particle mixtures to predict segregation in granular flows (Umbanhowar *et al.* 2019).

The predictions of (4.2) are obtained by first calculating $c = c(R)$ for each I (solid curves with blue to red colours in figure 8a) for fixed $R_\rho = 4$ according to (3.2) and then calculating the corresponding $w_i(R)$ (solid curves in figure 8b) according to (4.2). Good agreement between the predictions and the simulation results is obtained for all data series in figure 8(b), which confirms the applicability of our segregation velocity model (4.2) to gravity-driven segregation in uniform shear, at least for the density ratio, $R_\rho = 4$, that we consider. For a wider range of R_ρ, a rich variety of rising and sinking behaviours can occur depending on the combination of R and R_ρ (Félix & Thomas 2004; Jing *et al.* 2020), but this is not examined further in this work. Moreover, we highlight that the $w_i(R)$ curves in figure 8(b) exhibit a monotonic trend similar to the size ratio dependence of the segregation velocity in previous cyclic shear (Trewhela *et al.* 2021) and bedload transport studies (Chassagne *et al.* 2020; Rousseau *et al.* 2021), which demonstrates the potential relevance of our model to these different systems. It is also evident from figure 8(a) that, although the strength of the segregation force, $f(R)$, has a peak at $R \approx 2$ (Guillard *et al.* 2016; van der Vaart *et al.* 2018; Jing *et al.* 2020; Liu & Müller 2021), w_i increases monotonically with R due to the combined effects of $f(R)$ and $c(R)$ in equation (4.2). Finally, the increasing trend of $w_i(R)$ in figure 8(b) is based on results in the single intruder limit, whereas a somewhat different trend of the segregation velocity in size-bidisperse mixtures has been found, which increases with R but plateaus for $R \gtrsim 3$ (Schlick *et al.* 2015). This likely indicates the influence of an additional segregation mechanism (free sifting) in mixtures with relatively large size ratios ($R \gtrsim 3$), whereby fine particles can more readily percolate through the matrix of coarse particles.

5. Conclusions

In this paper, we use extensive DEM simulations to explore the net resistive drag force on a spherical intruder in uniformly-sheared dense granular flows in the absence of gravity. The simulations encompass a parameter space that is broader than explored previously, including drag forces $0.01 \leqslant F_d/(P_0 d_i^2) \leqslant 100$, inertial numbers $10^{-3} \lesssim I \lesssim 1$, intruder size ratios $0.6 \leqslant R \leqslant 5$, and intruder density ratios $1 \leqslant R_\rho \leqslant 20$. Three regimes of drag behaviour over the space defined by the dimensionless drag force $F_d/(P_0 d_i^2)$ and the dimensionless inertial number I are observed (figures 3c,e), including a fluctuation-dominated regime for small $F_d/(P_0 d_i^2)$ where it is difficult to accurately measure w_i in our simulation geometry, a viscous-like regime for intermediate $F_d/(P_0 d_i^2)$ where $F_d \propto w_i$, and an inertia-like regime for large $F_d/(P_0 d_i^2)$ where cavity formation occurs and the scaling relation transitions toward $F_d \propto w_i^2$; the transitional behaviour between the viscous and inertial scaling depends on I. Despite the variety of intruder dynamics displayed in these drag regimes, the viscous-like scaling remains relevant even when cavity formation occurs for a range of intermediate I due to the transition from viscous to inertial behaviour. The viscous-like scaling may also be relevant in the fluctuation-dominated regime, although

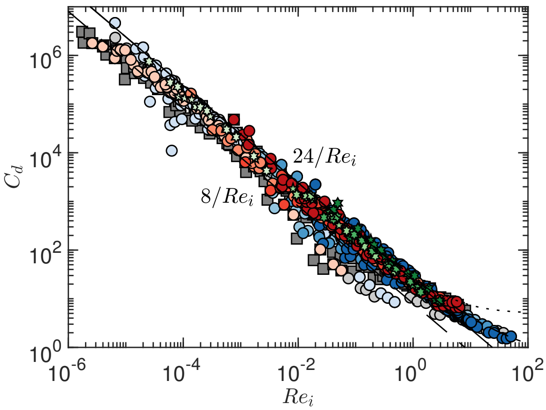

FIGURE 9. Summary of C_d vs. Re_i data for all $(I,\ R,\ R_\rho)$ conditions explored in this paper, including over 1000 simulations with $0.01 \leqslant F_d/(P_0 d_i^2) \leqslant 100$, $10^{-3} \lesssim I \lesssim 1$, $0.6 \leqslant R \leqslant 5$, and $1 \leqslant R_\rho \leqslant 20$. Symbol colours match those in figure 7, and the solid, dashed, dotted, and dot-dash model curves are identical to those in figures 4 and 6.

it is difficult to assess using our approach here due to the large fluctuations in the motion of intruder particles. Nevertheless, as a result of the dominance of the $F_d \propto w_i$ scaling, nearly all simulation results collapse onto a master curve, which can be described by a Stokesian drag model, $C_d = 8c/Re_i$, or $F_d = c\pi\eta d_i w_i$ (3.1), for Re_i spanning over five orders of magnitude ($10^{-5} \lesssim Re_i \lesssim 1$), as is summarized in figure 9, which includes all data from figures 4, 6, and 7. Even within the remarkable collapse of the data in figure 9, the value for the drag prefactor $c = c(I, R, R_\rho)$, which varies approximately from 1 to 3, can be described by an empirical expression (3.2).

The Stokesian drag model (3.1) developed here indicates a striking similarity between intruder drag in a granular flow and drag on a sphere in a viscous fluid. This also leads to a terminal velocity-like formulation for the intruder velocity (4.2) by combining the Stokesian drag model with a previously established Archimedean segregation force model for uniform shear flows (Jing *et al.* 2020). As discussed in §4.2, this "granular terminal velocity" captures the dependence of the intruder segregation velocity on the flow conditions and the particle size and density ratios, matching our simulation results of gravity-driven segregation of heavy intruders in uniform shear, as well as resembling some aspects of previous segregation studies using heap flow (Schlick *et al.* 2015; Xiao *et al.* 2016; Duan *et al.* 2021), cyclic shear (Trewhela *et al.* 2021), and bedload transport (Rousseau *et al.* 2021). Hence, although our drag model is developed in an idealized uniform shear flow in the absence of gravity for an isolated intruder, it appears to be relevant to more complicated granular shear flows where stress gradients and kinematics gradients exist. Indeed, our preliminary tests indicate that the drag coefficient is insensitive to the presence of gravity or an arbitrary shear rate gradient in the flow, using the velocity profile control approach of Jing *et al.* (2021). The insensitivity of the drag force to gradients in the flow is not surprising and is analogous to the drag in a viscous fluid. Nevertheless, future work should further confirm or extend the applicability of our model (3.1) in different granular flow configurations.

Despite the simplicity of our drag model and its effectiveness over a broad range of conditions, the model is not the complete answer and many research directions remain for developing a fuller understanding of drag in granular flows. First, it would be interesting to further explore the directionality of the intruder drag following the third discussion point in §4.1. Although we focus on the net intruder force and velocity in the z-direction, the streamwise (x) intruder velocity relative to the mean flow velocity may also affect the measured drag force by inducing lift effects in the z-direction (Ding *et al.* 2011; van der Vaart *et al.* 2018). The lift is likely more important if the net drag force has an angle with respect to the z-direction (see §4.1) or for a very heavy intruder which has significant inertia in the flow direction. Indeed, it may be useful to consider the intruder drag in both streamwise and depthwise directions as a coupled process, because typically the orientation of the contact forces on intruder particles is anisotropic (see, e.g., figure 1a inset) with a principal contact orientation unaligned with the shear direction (Azéma & Radjaï 2014; Jing *et al.* 2017; van Schrojenstein Lantman 2019; van Schrojenstein Lantman *et al.* 2021). Second, while we focus on granular flows well above yielding ($I > 10^{-3}$), non-local effects can also play a role in drag if I is further decreased toward the creeping flow regime (Candelier & Dauchot 2009; Nichol *et al.* 2010; Reddy *et al.* 2011; Zheng *et al.* 2018). In fact, the fluctuation-dominated regime in figure 2(a), which is a consequence of intermittency in the intruder dynamics, may be related to non-locality in granular materials (Kamrin 2019). Finally, from a practical standpoint, it is necessary to extend the current drag and segregation velocity models from the single intruder limit toward mixtures with finite particle concentrations, perhaps in a way similar to our recent work on the segregation driving force (Duan *et al.* 2022), thereby developing a more general framework for continuum modelling of granular segregation (Tripathi *et al.* 2021; Rousseau *et al.* 2021; Bancroft & Johnson 2021; Duan *et al.* 2022).

Acknowledgements

We thank Yi Fan, John Hecht, and Yifei Duan for valuable discussions. The research is facilitated in part by the computational resources and staff contributions provided by the Quest high performance computing facility at Northwestern University, which is jointly supported by the Office of the Provost, the Office for Research and Northwestern University Information Technology.

Funding

This material is based upon work supported by the National Science Foundation under Grant No. CBET-1929265.

Declaration of interests

The authors report no conflict of interest.

Appendix A. Uniform shear using force feedback

In this work, simple shear (figure 1a) is used to avoid segregation effects on the intruder that can occur due to pressure and shear gradients (Jing *et al.* 2021). However, uniform flow fields do not necessarily result for all flow conditions when simply translating the upper wall due to shear localization near the walls, especially for relatively thick flows (reaching about $35d$ in thickness here). To ensure uniform shear along the flow depth, we apply a small streamwise stabilizing force to each DEM particle (except the intruder) at each time step:

$$F_s = K_s[u(z_p) - u_p], \tag{A 1}$$

where z_p and u_p are the instantaneous particle position and velocity, respectively, and $u(z) = \dot{\gamma}_0 z$ is the desired uniform shear velocity profile. This velocity control approach has been adopted widely to study granular rheology (Lerner *et al.* 2012; Clark *et al.* 2018) and segregation (Fry *et al.* 2018; Duan *et al.* 2020) in uniform shear flows, but it can also be applied to explore arbitrarily non-uniform shear (Saitoh & Tighe 2019; Jing *et al.* 2021). The parameter K_s determines how much the stabilizing force affects the flow kinematics; it should be small enough to not alter the granular flow rheology and large enough to ensure satisfactory linear velocity profiles. However, the value of K_s has previously been determined in an ad hoc manner, depending on the flow conditions (Fry *et al.* 2018).

Here, we use a dimensional analysis to shed light on the appropriate range of K_s. The applied stabilizing forces on an assembly of particles can be viewed as an external force with strength proportional to the difference between the particle velocity and the desired velocity profile, and the latter is approximately the same as the mean steady-state flow velocity if the velocity control is effective. Therefore, at steady state, the mean stabilizing force is proportional to the velocity fluctuation of the flow; that is,

$$\langle F_s \rangle \propto K_s \sqrt{T}, \tag{A 2}$$

where $\langle \cdot \rangle$ denotes ensemble average, $T = (\delta u^2 + \delta v^2 + \delta w^2)/3$ is the granular temperature of the particle assembly (Weinhart *et al.* 2013), and $(\delta u, \delta v, \delta w)$ are the (x, y, z)-components of the velocity fluctuation. For dense granular flows, the velocity fluctuation (or, here, the square root of the granular temperature) follows a general scaling law,

$$\sqrt{T} \propto \dot{\gamma}_0 d I^{\alpha}, \tag{A 3}$$

where α is a system-dependent parameter (da Cruz *et al.* 2005; Rognon & Macaulay 2021; Kim & Kamrin 2020; Bancroft & Johnson 2021). Recent DEM simulations (Kim & Kamrin 2020; Bancroft & Johnson 2021) suggest $\alpha = -0.25$ for three-dimensional uniform shear flows, which approximately matches the slope of our uncontrolled (as well as weakly controlled) flow results in figure 10(a).

Substituting (A 3) into (A 2) and dividing both sides of (A 2) by a force scale $P_0 d^2$ results in

$$\frac{\langle F_s \rangle}{P_0 d^2} \propto \frac{K_s \dot{\gamma}_0 I^{\alpha}}{P_0 d}, \tag{A 4}$$

which indicates that the dimensionless stabilizing force, $\tilde{F}_s = \langle F_s \rangle/(P_0 d^2)$, is controlled by a dimensionless parameter $\tilde{K}_s = K_s \dot{\gamma}_0 I^{\alpha}/(P_0 d)$ and that $\tilde{F}_s$ characterizes the relative significance of the applied stabilizing force with respect to the mean contact force in the flow resulting from the applied pressure. Based on this understanding, we systematically vary $\tilde{K}_s$ as $\{0.01, 0.05, 0.1, 0.5, 1\}$ (from light to dark filled symbols in figure 10) for $10^{-3} \lesssim I \lesssim 1$ (same flow conditions as in figure 1) to determine the appropriate range for $\tilde{K}_s$. From figure 10(a), it is evident that values of $\tilde{K}_s$ that are too small produce similar results to uncontrolled flow (red crosses in figure 10a), while values of $\tilde{K}_s$ that are too large result in deviation from the $\alpha = -0.25$ slope, as the velocity fluctuation is over-modulated by $\tilde{F}_s$ (mainly in the x-direction along which $\tilde{F}_s$ is applied). For intermediate $\tilde{K}_s$, the data match nearly perfectly with the $\alpha = -0.25$ slope.

To assess if the velocity profile $u(z)$ is linear, we define a shape factor $\chi = \overline{u^2}/\bar{u}^2$ for each flow velocity profile, where the over-bar indicates depth averaging. We then compare χ with a reference value $\chi_0 = 4/3$, which represents a perfectly linear $u(z)$, in figure 10(b).

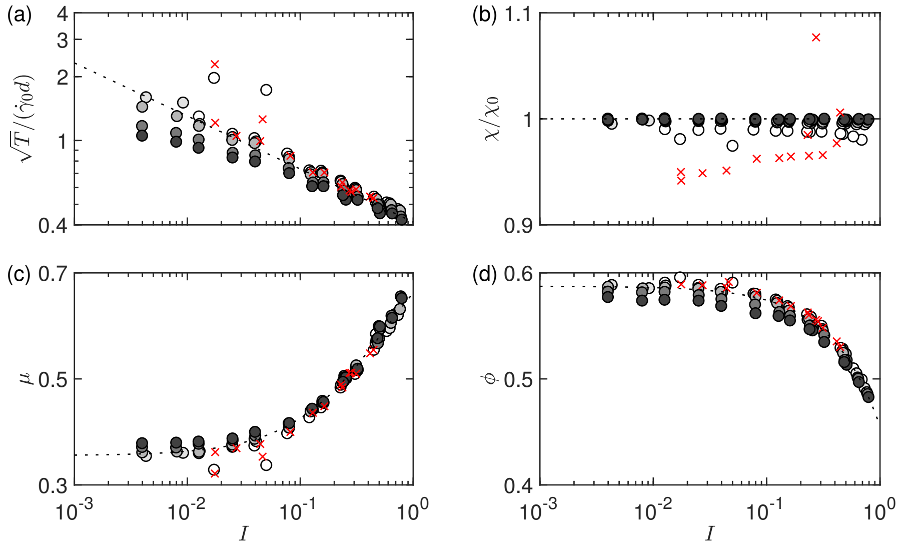

FIGURE 10. Effects of $\tilde{K}_s$ on (a) $\sqrt{T}/(\dot{\gamma}_0 d)$, (b) χ/χ_0, (c) μ, and (d) ϕ vs. I. Filled circles with light to dark shading are velocity-controlled flows with $\tilde{K}_s = \{0.01, 0.05, 0.1, 0.5, 1\}$, while red crosses are uncontrolled, simple shear flows ($\tilde{K}_s = 0$). The dotted lines in (a,b) indicate, respectively, a slope of -0.25 and a perfect linear velocity profile ($\chi/\chi_0 = 1$), while the dotted curves in (c,d) are empirical fits identical to the curves in figures 1(b,c). The flow properties T, μ, and ϕ are averaged in a $10d$-thick layer in the middle of the flow, while the shape factor χ is computed considering the entire velocity profile between the lower and upper bounding walls.

The χ/χ_0 results of uncontrolled, simple shear simulations (red crosses) exhibit clear deviations from $\chi/\chi_0 = 1$ (dotted line), indicating non-uniform shear. Likewise, $\tilde{K}_s = 0.01$ (weakly controlled flow) results in χ/χ_0 slightly less than one, which is expected because too small of a value for $\tilde{K}_s$ will not result in the desired linear velocity profile. By contrast, near-perfect uniform shear is achieved for $\tilde{K}_s \geqslant 0.05$.

Figures 10(c,d) show how the choice of $\tilde{K}_s$ affects the flow rheology in terms of the effective friction μ and packing density ϕ (measured in a $10d$ layer in the middle of the flow). The controlled flows with $\tilde{K}_s = \{0.05, 0.1, 0.5\}$ are not significantly affected, while smaller and larger values of $\tilde{K}_s$ lead to slight deviations from the typical rheology. Nevertheless, we have verified that the deviation does not affect the drag and segregation results in the z-direction, because the velocity control is applied only in the x-direction. Based on this assessment, we use $\tilde{K}_s = 0.1$ in our main simulations for the full range of I and note that increasing or decreasing $\tilde{K}_s$ by an order of magnitude does not alter the results.

Appendix B. Empirical fit of the $c = c(I, R, R_\rho)$ relation

It would be ideal to have a functional form for $c = c(I, R, R_\rho)$ to complement the Stokes-like drag model (3.1), but a theory-based approach is unclear due to the complex geometric and mass effects typical of dense granular flows (Liu & Müller 2021). Here, we propose an empirical model for $c = c(I, R, R_\rho)$ by exploiting the self-similar shape of the different data series in figure 7(b) and the linear correlations in figures 7(a,c). We first use an exponential function combined with a linear term, inspired by the shape of a regularized Bingham viscoplastic constitutive model (Papanastasiou & Boudouvis 1997), to fit the $I = 0.008$ data in figure 7(b),

$$c\big|_{R_\rho=1,I=0.008} = [k_1 - k_2 \exp(-k_3 R)] + k_4 R, \tag{B 1}$$

where $k_1 = 2$, $k_2 = 7$, $k_3 = 2.6$, and $k_4 = 0.005$ are fitting parameters specific to $I = 0.008$. Then, we fix k_1, k_2, and k_3 (for simplicity) and fit (B 1) to other data series in figure 7(b) to obtain k_4 for different I, which leads to

$$k_4 = s_1 I, \tag{B 2}$$

where $s_1 = 0.57$. Note that k_4, which depends linearly on I, is the slope of the asymptotic line for each curve in figure 7(b). This yields a function for c that depends on I,

$$c\big|_{R_\rho=1} = [k_1 - k_2 \exp(-k_3 R)] + s_1 I R, \tag{B 3}$$

which matches the $R = 1$ and $R = 4$ data (solid lines in figure 7a).

Finally, we assume that the effects of R and R_ρ are additive and that c depends linearly on R_ρ with a slope that is different for different I (see figure 7c), i.e.,

$$c = [k_1 - k_2 \exp(-k_3 R)] + s_1 I R + s_2 I (R_\rho - 1), \tag{B 4}$$

where $s_2 = 0.1$ is obtained by fitting (B 4) to each data series in figure 7(c). Note that (B 4) is identical to (3.2) in the main text and that (B 4) reduces to (B 3) when $R_\rho = 1$.

Figures 7(a–c) show that our empirical model (B 4) (solid curves) matches each data series (symbols with colour matching the corresponding curves), and, alternatively, the agreement is demonstrated in figure 7(d) by plotting the results of c from figures 7(a–c) against the values for c using (B 4) for all simulation conditions of (I, R, R_ρ). Moreover, the additivity assumption in (B 4) is confirmed in figure 7(d) by simulation results of simultaneously varied intruder size and density ratios, i.e., $(R, R_\rho) = (2, 5)$ and $(R, R_\rho) = (2, 10)$, for various inertial numbers ($I = \{0.008, 0.16, 0.32, 0.64\}$).

Appendix C. Connections with a previous drag model

Bancroft & Johnson (2021) developed a drag model using DEM simulations of density-bidisperse mixtures in a shear cell with Lees-Edwards boundary conditions,

$$c_{BJ} = \frac{b_i}{w_i} = \frac{\dot\gamma_0}{\kappa I^{7/4}}, \tag{C 1}$$

where c_{BJ} is a (dimensional) drag coefficient, b_i is the bulk acceleration acting on species i, w_i is the induced percolation velocity of species i, and $\kappa = 0.17$ is a fitting parameter.

A major difference between (C 1) and our approach is that instead of using an effective viscosity η to collapse data, Bancroft & Johnson (2021) directly correlated $c_{BJ}/\dot\gamma_0$ with I. To test if (C 1) is applicable to our data (see figure 11a caption) in the intruder limit, we redefine the intruder acceleration as $b_i = F_d/m_i$ and recast the data in figure 11(a) into $c_{BJ}/\dot\gamma_0$ vs. I in figure 11(b). Interestingly, this collapses the data for $R = 1$, leading to quantitative agreement with the scaling relation (C 1) (red solid curve). However, the results of varying R and R_ρ deviate systematically from (C 1) (see, e.g., the red dashed curve for $R = 4$). Therefore, it appears that the η-based scaling in figure 11(a) collapses the data for varying R and R_ρ better than the I-based scaling (C 1), although the two approaches produce similar data collapse for $R = 1$.

Another way to connect the two approaches is through our drag model (3.1). We first substitute $b_i = F_d/m_i = c\pi\eta d_i w_i/[(\pi/6)\rho_i d_i^3]$ into (C 1), leading to

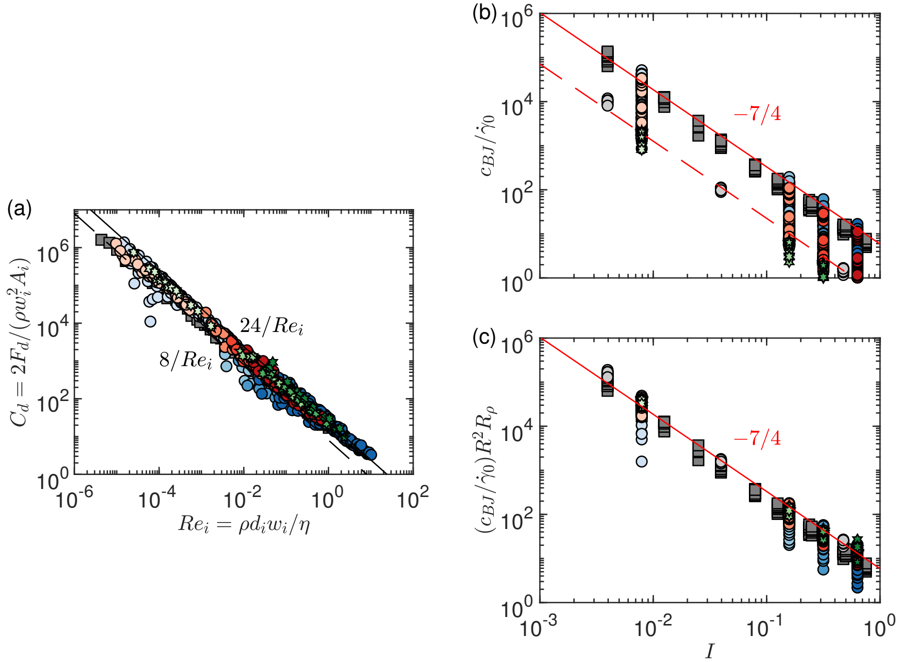

FIGURE 11. (a) Identical to figure 9 except that only the data associated with $0.1 \leqslant F_d/(P_0 d_i^2) \leqslant 5$ are included (about 800 simulations). (b,c) Data recast from (a), where the solid red curves are described by (C 1) and (C 3) with $\kappa = 0.17$ and $\kappa' = 0.17$, respectively. The dashed red curve in (b) has a slope of $-7/4$ and passes approximately through the $R = 4$ data (grey circles).

$$c_{BJ} = \frac{6c\eta}{\rho_i d_i^2}, \tag{C 2}$$

and then, noting that $\eta = \mu P_0/\dot{\gamma}_0$ and replacing P_0 by $\rho(\dot{\gamma}_0 d/I)^2$ based on the definition of I, we rearrange (C 2) into

$$c_{BJ} = \frac{6c\mu\rho(\dot{\gamma}_0 d/I)^2}{\rho_i d_i^2 \dot{\gamma}_0} = \frac{\dot{\gamma}_0}{\kappa' I^{7/4}} \frac{1}{R^2 R_\rho}, \tag{C 3}$$

where $\kappa' = I^{1/4}/(6c\mu)$. The resulting scaling, $(c_{BJ}/\dot{\gamma}_0)R^2R_\rho \propto I^{-7/4}$, collapses all data reasonably well in figure 11(c). Noting that $c = c(I, R, R_\rho)$, we have $\kappa' = \kappa'(I, R, R_\rho)$, which explains why the data collapse for varying R and R_ρ is imperfect in figure 11(c).

REFERENCES

ALBERT, R., PFEIFER, M. A., BARABÁSI, A.-L. & SCHIFFER, P. 1999 Slow drag in a granular medium. *Phys. Rev. Lett.* **82** (1), 205–208.

AZÉMA, EMILIEN & RADJAÏ, FARHANG 2014 Internal structure of inertial granular flows. *Phys. Rev. Lett.* **112** (7), 078001.

BANCROFT, R. S.J. & JOHNSON, C. G. 2021 Drag, diffusion and segregation in inertial granular flows. *J. Fluid Mech.* **924**, A3.

CANDELIER, R. & DAUCHOT, O. 2009 Creep motion of an intruder within a granular glass close to jamming. *Phys. Rev. Lett.* **103** (12), 128001.

CHASSAGNE, R., MAURIN, R., CHAUCHAT, J., GRAY, J. M. N. T. & FREY, P. 2020 Discrete and continuum modelling of grain size segregation during bedload transport. *J. Fluid Mech.* **895**, A30.

Clark, A. H., Petersen, A. J. & Behringer, R. P. 2014 Collisional model for granular impact dynamics. *Phys. Rev. E* **89** (1), 012201.

Clark, A. H., Thompson, J. D., Shattuck, M. D., Ouellette, N. T. & O'Hern, C. S. 2018 Critical scaling near the yielding transition in granular media. *Phys. Rev. E* **97** (6), 062901.

da Cruz, F., Emam, S., Prochnow, M., Roux, J. & Chevoir, F. 2005 Rheophysics of dense granular materials: discrete simulation of plane shear flows. *Phys. Rev. E* **72**, 021309.

Das, P., Puri, S. & Schwartz, M. 2020 Intruder dynamics in a frictional granular fluid: A molecular dynamics study. *Phys. Rev. E* **102** (4), 042905.

Ding, Y., Gravish, N. & Goldman, D. I. 2011 Drag induced lift in granular media. *Phys. Rev. Lett.* **106** (2), 028001.

Duan, Y., Jing, L., Umbanhowar, P. B., Ottino, J. M. & Lueptow, R. M. 2022 Segregation forces in dense granular ows: closing the gap between single intruders and mixtures. *J. Fluid Mech.* **935**, R1.

Duan, Y., Umbanhowar, P. B., Ottino, J. M. & Lueptow, R. M. 2020 Segregation models for density-bidisperse granular flows. *Phys. Rev. Fluids* **5** (4), 044301.

Duan, Y., Umbanhowar, P. B., Ottino, J. M. & Lueptow, R. M. 2021 Modelling segregation of bidisperse granular mixtures varying simultaneously in size and density for free surface flows. *J. Fluid Mech.* **918**, A20.

Félix, G. & Thomas, N. 2004 Evidence of two effects in the size segregation process in dry granular media. *Phys. Rev. E* **70** (5), 051307.

Forterre, Y. & Pouliquen, O. 2008 Flows of dense granular media. *Annu. Rev. Fluid Mech.* **40** (1), 1–24.

Fry, A. M., Umbanhowar, P. B., Ottino, J. M. & Lueptow, R. M. 2018 Effect of pressure on segregation in granular shear flows. *Phys. Rev. E* **97** (6), 062906.

Geng, J. & Behringer, R. P. 2005 Slow drag in two-dimensional granular media. *Phys. Rev. E* **71** (1), 011302.

Goossens, W. R. A. 2019 Review of the empirical correlations for the drag coefficient of rigid spheres. *Powder Tech.* **352**, 350–359.

Gravish, N., Umbanhowar, P. B. & Goldman, D. I. 2010 Force and flow transition in plowed granular media. *Phys. Rev. Lett.* **105** (12), 128301.

Gray, J. M. N. T. 2018 Particle segregation in dense granular flows. *Annu. Rev. Fluid Mech.* **50** (1), 407–433.

Guillard, F., Forterre, Y. & Pouliquen, O. 2016 Scaling laws for segregation forces in dense sheared granular flows. *J. Fluid Mech.* **807**, R1.

Jenkins, J. T. & Yoon, D. K. 2002 Segregation in binary mixtures under gravity. *Phys. Rev. Lett.* **88** (19), 194301.

Jing, L., Kwok, C. Y. & Leung, Y. F. 2017 Micromechanical origin of particle size segregation. *Phys. Rev. Lett.* **118** (11), 118001.

Jing, L., Kwok, C. Y., Leung, Y. F. & Sobral, Y. D. 2016 Characterization of base roughness for granular chute flows. *Phys. Rev. E* **94** (5), 052901.

Jing, L., Ottino, J. M., Lueptow, R. M. & Umbanhowar, P. B. 2020 Rising and sinking intruders in dense granular flows. *Phys. Rev. Res.* **2** (2), 022069.

Jing, L., Ottino, J. M., Lueptow, R. M. & Umbanhowar, P. B. 2021 A unified description of gravity- and kinematics-induced segregation forces in dense granular flows. *J. Fluid Mech.* **925**, A29.

Kamrin, K. 2019 Non-locality in granular flow: Phenomenology and modeling approaches. *Front. Phys.* **7**, 116.

Kim, S. & Kamrin, K. 2020 Power-law scaling in granular rheology across flow geometries. *Phys. Rev. Lett.* **125** (8), 088002.

Lerner, E., Düring, G. & Wyart, M. 2012 A unified framework for non-Brownian suspension flows and soft amorphous solids. *Proc. Natl. Acad. Sci. U.S.A.* **109** (13), 4798–4803.

Li, C., Zhang, T. & Goldman, D. I. 2013 A terradynamic of legged locomotion on granular media. *Science* **339** (6126), 1408–1412.

Liu, M. & Müller, C. R. 2021 Lift force acting on an intruder in dense, granular shear flows. *Phys. Rev. E* **104** (6), 064903.

Liu, S. & McCarthy, J. J. 2017 Transport analogy for segregation and granular rheology. *Phys. Rev. E* **96** (2), 020901(R).

Nichol, K., Zanin, A., Bastien, R., Wandersman, E. & van Hecke, M. 2010 Flow-induced agitations create a granular fluid. *Phys. Rev. Lett.* **104** (7), 078302.

Pacheco-Vázquez, F. & Ruiz-Suárez, J.C. 2010 Cooperative dynamics in the penetration of a group of intruders in a granular medium. *Nat. Commun.* **1** (8), 123.

Papanastasiou, T. C. & Boudouvis, A. G. 1997 Flows of viscoplastic materials: Models and computations. *Comput. Struct.* **64** (1), 677–694.

Reddy, K. A., Forterre, Y. & Pouliquen, O. 2011 Evidence of mechanically activated processes in slow granular flows. *Phys. Rev. Lett.* **106** (10).

Rognon, P. & Macaulay, M. 2021 Shear-induced diffusion in dense granular fluids. *Soft Matter* **17** (21), 5271–5277.

Rousseau, H., Chassagne, R., Chauchat, J., Maurin, R. & Frey, P. 2021 Bridging the gap between particle-scale forces and continuum modelling of size segregation: application to bedload transport. *J. Fluid Mech.* **916**, A26.

Saitoh, K. & Tighe, B. P. 2019 Nonlocal effects in inhomogeneous flows of soft athermal disks. *Phys. Rev. Lett.* **122** (18), 188001.

Schlichting, H. T. 1979 *Boundary-Layer Theory*, 7th edn. McGraw-Hill.

Schlick, C. P., Fan, Y., Isner, A. B., Umbanhowar, P. B., Ottino, J. M. & Lueptow, R. M. 2015 Modeling segregation of bidisperse granular materials using physical control parameters in the quasi-2d bounded heap. *AIChE J.* **61** (5), 1524–1534.

van Schrojenstein Lantman, M. P. 2019 A study on fundamental segregation mechanisms in dense granular flows. PhD, University of Twente, Enschede, The Netherlands.

van Schrojenstein Lantman, M. P., van der Vaart, K., Luding, S. & Thornton, A. R. 2021 Granular buoyancy in the context of segregation of single large grains in dense granular shear flows. *Phys. Rev. Fluids* **6** (6), 064307.

Seguin, A., Bertho, Y., Martinez, F., Crassous, J. & Gondret, P. 2013 Experimental velocity fields and forces for a cylinder penetrating into a granular medium. *Phys. Rev. E* **87** (1), 012201.

Seguin, A. & Gondret, P. 2017 Drag force in a cold or hot granular medium. *Phys. Rev. E* **96** (3), 032905.

Staron, L. 2018 Rising dynamics and lift effect in dense segregating granular flows. *Phys. Fluids* **30** (12), 123303.

Stone, M. B., Bernstein, D. P., Barry, R., Pelc, M. D., Tsui, Y.-K. & Schiffer, P. 2004 Stress propagation: Getting to the bottom of a granular medium. *Nature* **427** (6974), 503–504.

Thornton, A. 2021 A brief review of (multi-scale) modelling approaches to segregation. *EPJ Web Conf.* **249**, 01004.

Trewhela, T., Ancey, C. & Gray, J. M. N. T. 2021 An experimental scaling law for particle-size segregation in dense granular flows. *J. Fluid Mech.* **916**, A55.

Tripathi, A. & Khakhar, D. V. 2011 Numerical simulation of the sedimentation of a sphere in a sheared granular fluid: A granular Stokes experiment. *Phys. Rev. Lett.* **107** (10), 108001.

Tripathi, A. & Khakhar, D. V. 2013 Density difference-driven segregation in a dense granular flow. *J. Fluid Mech.* **717**, 643–669.

Tripathi, A., Kumar, A., Nema, M. & Khakhar, D. V. 2021 Theory for size segregation in flowing granular mixtures based on computation of forces on a single large particle. *Phys. Rev. E* **103** (3), L031301.

Umbanhowar, P. B., Lueptow, R. M. & Ottino, J. M. 2019 Modeling segregation in granular flows. *Annu. Rev. Chem. Biomol. Eng.* **10** (1), 5.1–5.25.

van der Vaart, K., van Schrojenstein Lantman, M. P., Weinhart, T., Luding, S., Ancey, C. & Thornton, A. R. 2018 Segregation of large particles in dense granular flows suggests a granular Saffman effect. *Phys. Rev. Fluids* **3** (7), 074303.

Weinhart, T., Hartkamp, R., Thornton, A. R. & Luding, S. 2013 Coarse-grained local and objective continuum description of three-dimensional granular flows down an inclined surface. *Phys. Fluids* **25** (7), 070605.

White, F. M. 1974 *Viscous Fluid Flow*, 1st edn. McGraw-Hill.

Xiao, H., Umbanhowar, P. B., Ottino, J. M. & Lueptow, R. M. 2016 Modelling density segregation in flowing bidisperse granular materials. *Proc. R. Soc. A.* **472** (2191), 20150856.

Zheng, H., Wang, D., Barés, J. & Behringer, R. P. 2018 Sinking in a bed of grains activated by shearing. *Phys. Rev. E* **98** (1), 010901.